A comparison of auroral oval proxies with the boundaries of the auroral electrojets

Simon James Walker[1], Karl Laundal[2], Jone Peter Reistad[3], Anders Ohma[4], Spencer Mark Hatch[5], Gareth Chisham[6], and Margot Decotte[7]

[1]Univerisity of Bergen
[2]University in Bergen
[3]Birkeland Centre for Space Science, University of Bergen
[4]Birkeland Centre for Space Science, Department of Physics and Technology, University of Bergen
[5]Birkeland Centre for Space Science
[6]British Antarctic Survey
[7]University of Bergen

January 13, 2024

Abstract

The boundaries of the auroral oval and auroral electrojets are an important source of information for understanding the coupling between the solar wind and the near-earth plasma environment. Of these two types of boundaries the auroral electrojet boundaries have received comparatively little attention, and even less attention has been given to the connection between the two. Here we introduce a technique for estimating the electrojet boundaries, and other properties such as total current and peak current, from 1-D latitudinal profiles of the eastward component of equivalent current sheet density. We apply this technique to a preexisting database of such currents along the 105* magnetic meridian producing a total of eleven years of 1 minute resolution electrojet boundaries during the period 2000–2020. Using statistics and conjunction events we compare our electrojet boundary dataset with an existing electrojet boundary dataset, based on Swarm satellite measurements, and auroral oval proxies based on particle precipitation and field aligned currents. This allows us to validate our dataset and investigate the feasibility of an auroral oval proxy based on electrojet boundaries. Through this investigation we find the proton precipitation auroral oval is a closer match with the electrojet boundaries. However, the bimodal nature of the electrojet boundaries as we approach the noon and midnight discontinuities makes an average electrojet oval poorly defined. With this and the direct comparisons differing from the statistics, defining the proton auroral oval from electrojet boundaries across all local and universal times is challenging.

A comparison of auroral oval proxies with the boundaries of the auroral electrojets

Simon James Walker[1], Karl Magnus Laundal [1], Jone Peter Reistad[1], Anders Ohma[1], Spencer Mark Hatch[1], Gareth Chisham[2], Margot Decotte[1]

[1]Department of Physics and Technology, University of Bergen, Norway
[2]British Antarctic Survey, Cambridge, UK

Key Points:

- We present a new electrojet boundary dataset and compare it with auroral oval proxies
- On average proton aurora boundaries are more aligned with electrojet boundaries than electron aurora boundaries
- Noon and midnight electrojet discontinuities present a problem for auroral oval determination from electrojet boundaries

Corresponding author: Simon Walker, `simon.walker@uib.no`

Abstract

The boundaries of the auroral oval and auroral electrojets are an important source of information for understanding the coupling between the solar wind and the near-earth plasma environment. Of these two types of boundaries the auroral electrojet boundaries have received comparatively little attention, and even less attention has been given to the connection between the two. Here we introduce a technique for estimating the electrojet boundaries, and other properties such as total current and peak current, from 1-D latitudinal profiles of the eastward component of equivalent current sheet density. We apply this technique to a preexisting database of such currents along the 105° magnetic meridian producing a total of eleven years of 1 minute resolution electrojet boundaries during the period 2000–2020. Using statistics and conjunction events we compare our electrojet boundary dataset with an existing electrojet boundary dataset, based on *Swarm* satellite measurements, and auroral oval proxies based on particle precipitation and field aligned currents. This allows us to validate our dataset and investigate the feasibility of an auroral oval proxy based on electrojet boundaries. Through this investigation we find the proton precipitation auroral oval is a closer match with the electrojet boundaries. However, the bimodal nature of the electrojet boundaries as we approach the noon and midnight discontinuities makes an average electrojet oval poorly defined. With this and the direct comparisons differing from the statistics, defining the proton auroral oval from electrojet boundaries across all local and universal times is challenging.

Plain Language Summary

The global location of the northern and southern lights holds particular importance for understanding where space weather hazards are heightened and where energy from space is deposited in the upper atmosphere. The brightness of these lights and related electrical currents also indicate the magnitude of the energy deposition and associated space weather hazards. However, global imaging of aurora is limited by sunlight, with generally fewer observations during summer months. Furthermore, global observations are not possible from the ground, and space based global imaging has been missing for close to two decades. In this study we investigate alternative methods, with particular emphasis on a technique based on ground magnetometers. Electrical currents have been robustly mapped for two decades over Fennoscandia, without observational limitations due to season. We investigate how the average location of these currents relate to the average location of the aurora and other related current systems. We use these results to discuss the feasibility of finding the location of the aurora from a more abundant data source and increasing the understanding of the underlying mechanisms.

1 Introduction

The boundaries of the auroral oval are natural points of reference for understanding and organising polar ionospheric electrodynamics (Burrell et al., 2020; Kilcommons et al., 2017; Andersson et al., 2004; Redmon et al., 2010). The poleward boundary of the auroral oval is a commonly used proxy of the boundary between open and closed magnetic field lines (OCB) and, therefore, can be used to determine the amount of open magnetic flux contained within the polar cap and is commonly used to describe the magnetic energy stored in the magnetotail (Milan et al., 2007, 2017). The equatorward boundary describes the extent of where this additional energy translates into enhanced auroral activity (precipitation, strengthened auroral electrojets etc.) and is important in understanding where space weather hazards are heightened (Carbary, 2005). The auroral electrojets are often described as flowing within the auroral oval (Johnsen, 2013) and measurements of the electrojets are often reduced to singular metrics to describe the state of polar ionospheric activity (i.e., Auroral Lower index, Auroral Upper index, etc.) (Kamide & Akasofu, 1983; Rostoker et al., 1980).

The auroral oval is typically phenomenologically defined by auroral emissions or through the populations of energetic particle precipitation (Longden et al., 2010; Chisham et al., 2022; Kilcommons et al., 2017; Decotte et al., 2023; Feldstein & Starkov, 1967; Holzworth & Meng, 1975; Zou et al., 2012). Thresholds of the total precipitating electron energy flux are an often used proxy of the OCB (Boakes et al., 2008; Longden et al., 2010). However, ground-based auroral observations, which began prior to the advent of space-based observations, are limited by location and condition requirements, such as clouds, lunar illumination and solar illumination. A number of satellite auroral observations are able to image the entire auroral oval and therefore can provide global boundaries, however they are limited by the time when the satellite was in operation, satellite orbit and to some extent solar illumination because of dayglow (Ohma et al., 2023). Particle detectors onboard satellites, such as the Defense Meteorlogical Space Program (DMSP) satellites, have enabled routine determination of auroral oval boundaries through identification of auroral particle precipitation populations (Kilcommons et al., 2017). An advantage of these measurements is they are not restricted by dayglow and solar illumination but they are limited to point observations along the satellite path. Decotte et al. (2023) have also shown that auroral boundaries identified via DMSP SSJ electrostatic analysers are biased in some local time sectors due to the trajectory of these satellites through the auroral zone.

Both field aligned currents and the auroral electrojets can be estimated from their magnetic field signatures using magnetometers onboard satellites such as CHAllenging Minisatellite Payload (CHAMP) and the *Swarm* satellites and have been compared with the auroral oval (Feldstein et al., 1999; Xiong & Lühr, 2014). Routines have been designed to find the FAC boundaries and electrojet boundaries, with advantages and disadvantages similar to those of boundary estimates made using satellite-based particle instruments (Xiong et al., 2014; Xiong & Lühr, 2014; Aakjær et al., 2016; Juusola et al., 2006; Viljanen et al., 2020; Kervalishvili et al., 2020). Historically, however, estimates of the electrojets have predominantly been made using ground based magnetometers (Harang, 1946). Like satellite magnetometers, ground-based magnetometers are not challenged by weather and solar illumination but additionally have the advantage of being fixed geographically (i.e., can remain in and around the auroral zone and ionospheric interaction region). Such measurements have generally been made at 1-min cadence for the last few decades, and more recently 10-s and even 1-s cadence. However, accurate background magnetic field estimates are required for baseline removal in order to retrieve the real magnitude of perturbations. Additionally, ground magnetometers are limited by location and operation, where more inaccessible sites generally experience more down time and areas of sea or completely inaccessible areas of land produce gaps in the distribution of magnetometers. Furthermore, ground induced currents can obscure the derivation of the ionospheric current particularly when it is assumed the magnetic field perturbations are purely of ionospheric origin.

The clear advantages of ground based magnetometers, in terms of data coverage and reliability, make it important to use the measurements to identify the boundaries of the auroral electrojets and understand their place in describing the auroral oval. Thus enhancing our knowledge of the auroral oval when more typical measurements are lacking and gaining a greater understanding of the links between ionospheric processes. To our knowledge, three studies have used an algorithm based approach to identify the boundaries of the auroral electrojets on the basis of ground magnetometer measurements (Kisabeth & Rostoker, 1971; Johnsen, 2013; Feldstein et al., 1999). In all of these studies the radial component of magnetic field perturbations was primarily used for determination of the latitudinal extent of the auroral electrojets, and in only one of these was a limited comparison with auroral oval boundaries carried out (Feldstein et al., 1999). Kisabeth and Rostoker (1971) used a set of magnetometers around the 302° magnetic meridian (Western Canada), and defined the boundaries of the auroral electrojet as the location of the maxima and minima in the radial component that flank the zero point of the ra-

Boundary Data Set	**Boundary Type**	**Measurements**
Current Paper (GBM) (S. J. Walker et al., 2023)	Auroral Electrojets	Ground Based Magnetometers (S. J. Walker et al., 2022; S. Walker et al., 2023)
Swarm (SBM) (Viljanen et al., 2020)	Auroral Electrojets	*Swarm* Magnetometers (Kervalishvili et al., 2020)
SI12 (Chisham et al., 2022)	Aurora	Space Based Imager (IMAGE)
SI13 (Chisham et al., 2022)	Aurora	Space Based Imager (IMAGE)
DMSP (Kilcommons et al., 2017)	Precipitation	Space Based Particle Detector
CHAMP Model (Xiong & Lühr, 2014)	Field Aligned Currents	CHAMP Magnetometer (Xiong et al., 2014)

Table 1: The data sets used in this study, the type of boundaries they identify, and the the measurements used to derive them.

dial component or the peak in the horizontal component. They investigated how the width and peak varied during a selection of substorms. Johnsen (2013) modelled the auroral electrojet as a set of line currents, with amplitudes obtained from fits to the ground magnetic field measured by ground magnetometers in Scandinavia. They then estimated the electrojet boundaries algorithmically using the same criteria described by Kisabeth and Rostoker (1971). These boundaries are then provided to real time tracking and alerts for auroral activity, such as the Advanced Forecast For Ensuring Communications Through Space (AFFECTS) project (Bothmer et al., 2013).

In Section 2 we estimate the electrojet boundaries from minute resolution electrojet current profiles along the 105° magnetic meridian presented by S. Walker et al. (2023) (S. J. Walker et al., 2022), which yields a database spanning a total of eleven years during the 21-year period between 2000 and 2020 (S. J. Walker et al., 2023). In Section 3 we compare these boundaries both in case studies and statistically with auroral electrojet boundaries estimated via satellite-bourne magnetometers, auroral oval boundaries found using particle precipitation measurements from DMSP satellites (Kilcommons et al., 2017; Decotte et al., 2023), a merging electric field scaled model of the FAC boundaries (Xiong et al., 2014; Xiong & Lühr, 2014) and auroral oval boundaries found using satellite based far ultra violet (FUV) measurements of the aurora (Longden et al., 2010; Chisham et al., 2022). In Section 4 we discuss these comparisons and how the auroral electrojet boundaries relate to the auroral oval both on average and on a case by case basis.

2 Data and Methodology

In this section we describe the different boundary datasets used in this study and the methodology behind them. Table 1 summarises these datasets. We also describe the parameters we use to bin our data.

2.1 Electrojet Boundaries from Regionally Constrained Divergence Free Currents

We now describe how we derive the database of electrojet boundaries and properties based on the minute-resolution sheet current density profiles produced by S. Walker et al. (2023).

2.1.1 Estimating the Electrojet Currents

The core component of S. Walker et al. (2023) and how they estimate the divergence-free ionospheric currents is the spherical elementary current systems (SECS) method. The superposition of an appropriately scaled collection of SECS basis functions can recreate any two-dimensional current system that exists on a spherical shell, such as the divergence-free ionospheric currents (Vanhamäki & Juusola, 2020; Amm, 1997; Amm & Viljanen, 1999). Amm (1997) introduced divergence-free SECS basis functions with this purpose in mind, and described the current associated with each type of basis function. Amm and Viljanen (1999) then derived analytic expressions for the corresponding magnetic field. These expressions for the magnetic field enable estimation of the amplitude of each member of a collection of SECS basis functions from measurements of the magnetic field via a linear inverse problem. Once these amplitudes are known, it is straightforward to calculate the total divergence-free current system that can represent the measured magnetic field. S. Walker et al. (2023) used measurements made by a fixed set of twenty ground magnetometers in Fennoscandia to constrain their SECS model along with regularisation of the east-west gradient and the amplitude of the model vector. Using this model, the divergence-free ionospheric sheet current density was estimated along the 105° magnetic meridian for each minute when the magnetometers were available concurrently over the twenty year period from 2000 to 2020 (S. J. Walker et al., 2022).

2.1.2 Electrojet Algorithm

We now describe the algorithm we use to estimate the boundaries and properties of the auroral electrojets (S. J. Walker et al., 2022) from the eastward component of the divergence-free current density for each of the sheet current density profiles described in the previous subsection. Examples of the eastward and westward electrojet boundaries identified via this algorithm are shown in the right middle panels of Figures 1 and 2. These figures show occurrences of DMSP and *Swarm* satellites coinciding with data from S. J. Walker et al. (2022) and a median sheet current density profile is created for each satellite by selecting data from S. J. Walker et al. (2022) that occurs between the time of the boundaries detected by the satellites during the event. Specifically, the algorithm estimates the poleward and equatorward boundary, the value and location of the peak sheet current, and the width and total current of multiple current sections, and proceeds as follows.

1. Initial boundary estimates are identified as the points where the current profile crosses positive or negative thresholds defined as the 10th percentile of the absolute current density or the latitude limits of the meridian (shown as thick black horizontal lines in the right middle panels of figure 1 and 2 as thresholds for the red median profile). This procedure splits the current profile into different sections.
2. Since the current profiles quite often flatten just above the 10th percentile, in the next step the boundary is moved closer to where a clear peak is formed. This point is defined as the closest point to the peak where the gradient is still less than 60% of the mean absolute gradient in the electrojet section. The peak itself is excluded by ensuring that the current magnitude is less than 40% of the mean of the particular section. If a new boundary can not be defined in this way, the initial estimate is kept. As such, the boundaries sometimes end up at or close to the low- and high-latitude edges of the meridian (respectively 49° and 81°). In such cases

the full current section may not have been resolved and the boundaries should not be used.

The boundaries (shown as vertical lines in Figure 1 and 2), peaks, widths, and total integrated current of the three strongest eastward and three strongest westward currents are saved, where the strength is defined by the total integrated current of the profile (the strongest east and west current sections are highlighted in Figure 1 and 2, with their corresponding colour, for the median profiles associated with the *Swarm* A satellite). This dataset is publicly available: S. J. Walker et al. (2023). In this study we use the following criteria to deselect a number of boundaries deemed untrustworthy:

1. Boundaries occurring on first three (less than 50.5° MLat) and last three meridian data points (greater than 79.5°) are removed as the entire current section may not have been resolved
2. Eastward (westward) current sections must have peaks greater than 0.05 Am^{-1} (less than -0.1 Am^{-1}) for their boundaries to remain. The thresholds are different because the westward electrojet is typically stronger than the eastward electrojet.

2.2 Swarm

We now outline the methodology of Aakjær et al. (2016), which is based on the work of Olsen (1996), for calculating sheet currents using *Swarm* magnetometers. This is the methodology used by Kervalishvili et al. (2020) to produce the publicly available sheet current dataset. That can be obtained from `https://vires.services/` using the code SW_OPER_AEJALPL_2F, SW_OPER_AEJBLPL_2F, and SW_OPER_AEJCLPL_2F for *Swarm* A, B and C respectively. We also describe how Viljanen et al. (2020) and Kervalishvili et al. (2020) use these sheet current profiles to create a data set of Swarm-based electrojet boundaries (also available from `https://vires.services/` using the code SW_OPER_AEJAPBL_2F, SW_OPER_AEJBPBL_2F, SW_OPER_AEJCPBL_2F for *Swarm* A, B and C respectively).

Aakjær et al. (2016) represent the auroral electrojet as a series of line currents at an altitude of approximately 110 km separated by 113 km along and orientated perpendicular to the satellite track. Similar to the SECS approach, the amplitude of each line current is obtained as an inverse problem in which the superimposed magnetic field of the line currents is constrained by the magnitude of the magnetic field perturbations measured by the *Swarm* satellites, where the contribution from FACs is minimal. In Viljanen et al. (2020) these line currents are then transformed into the Quasi-Dipole magnetic east direction before applying the following electrojet algorithm:

1. Find the interpolated zero crossings of the current density curve.
2. Calculate the total current between crossings.
3. Define the electrojet as the series of current densities with the maximum total current or minimum in the case of the westward electrojet.

The dataset is also provided with a set of quality flags that allow for the removal of spurious boundaries. In this study the quality flags were used to remove bad boundaries if any of the following conditions are true:

1. No eastward/westward currents detected.
2. The equatorward boundary occurs at the edge of the analysis area and the density is larger than 20% of peak value.
3. The poleward boundary occurs at the edge of the analysis area and the density is larger than 20% of peak value.

4. the *Swarm* orbit does not fully cover the predefined oval latitude range. The latitude gap is 2 degrees or larger.
5. The equatorward boundary occurs at the edge of the analysis area.
6. The poleward boundary occurs at the edge of the analysis area.
7. The peak value occurs at the edge of the analysis area.

As both an eastward and westward electrojet can be detected in one oval crossing and only the peaks of the electrojets are provided, we choose the appropriate electrojet by the one with the largest peak magnitude.

2.3 Xiong FAC Boundaries

Xiong et al. (2014) use the magnetic field measurements made by CHAllenging Minisatellite Payload (CHAMP) to estimate small-scale field-aligned currents (FACs). They then use these estimates to identify the boundaries of the FACs for each pass of the auroral oval. Xiong and Lühr (2014) bin these boundaries based on MLT and time integrated merging electric field (E_m), with the latter defined in terms of the Newell epsilon value (Newell et al., 2007). For each E_m bin an ellipse is fit to the mean latitude of the poleward and equatorward boundaries across all MLT bins. Each ellipse parameter is represented by a quadratic in terms of E_m, with coefficients estimated using least squares, thus creating a model of the FAC boundaries that is dependent on the Newell epsilon parameter.

2.4 Boundaries from Global Auroral Imagery

Longden et al. (2010) and Chisham et al. (2022) define an algorithm for identifying auroral boundaries in FUV images from the Imager for Magnetopause-to-Aurora Global Exploration (IMAGE) satellite (Mende, Heetderks, Frey, Lampton, et al., 2000). They apply this algorithm to all three imagers on the IMAGE satellite, SI12, SI13 and WIC, creating three datasets. For this study we focus on the boundaries found using the SI12 and SI13 imagers (Mende, Heetderks, Frey, Stock, et al., 2000), which measure emissions related to proton and electron precipitation respectively, as they have a reduced influence from dayglow compared to the WIC imager (Longden et al., 2010). The Chisham et al. (2022) auroral boundary algorithm proceeds as follows: (1) The locations of the pixels of the raw image are found in AACGM (Altitude Adjusted Corrected Geomagnetic) coordinates. (2) Measured intensities in the image are subdivided into bins of size 1 h in MLT, the first bin being 0–1 MLT, and 1° MLat between 50° and 90° MLat. (3) A latitudinal intensity profile is constructed for each MLT segment. (4) This profile is then fitted by two different functions: the sum of a Gaussian function and a quadratic, and the sum of two Gaussian functions and a quadratic. The function with better goodness of fit is then chosen as the better fit. (5) In the case of a single Gaussian being the better fit the poleward and equatorward boundaries are determined by the peak of the Gaussian curve plus and minus the full width at half maximum (FWHM) of the Gaussian respectively. In the case of the double Gaussian the poleward boundary is determined by the peak of the Gaussian curve with the poleward maximum plus its FWHM and the equatorward boundary is determined by the peak of the Gaussian curve with the equatorward maximum minus its FWHM. Additional acceptance criteria for a successful boundary determination can be found in Longden et al. (2010) and Chisham et al. (2022).

2.5 DMSP (Kilcommons Algorithm)

The Kilcommons et al. (2017) algorithm estimates the auroral oval boundaries on the basis of precipitation measurements made by the Special Sensor J (SSJ) instrument onboard DMSP satellites. Decotte et al. (2023) use a portion of this algorithm to produce auroral precipitation occurrence probability maps from the same measurements.

Using the total energy flux of electrons between 1.3 and 30 keV (J_E), Kilcommons et al. (2017) identify candidate auroral ovals as regions where J_E is greater than 10^9 eV for polar passes that cross the auroral oval in two places. Using a figure of merit an auroral oval pair is selected from the candidates and the latitude limits recorded as auroral oval boundaries. Examples of these boundaries can be seen in the top right panel of Figure 1 and 2 along with the J_E latitude profile.

Decotte et al. (2023) used a similar approach however, they use a limit of 2×10^9 eV. Furthermore, to counter problems due to orbital bias and make a dataset that can be statistically compared to the others mentioned in the prior subsections, the threshold is used to create a binary dataset of spacecraft locations (for several DMSP satellites) defined as being within either auroral or non auroral precipitation. From this dataset statistical maps of auroral precipitation occurrence probability are then created.

2.6 Newell coupling function ϵ_N

We make use of the Newell coupling function

$$\epsilon_N = v^{4/3}\left(\sqrt{B_y^2+B_z^2}\right)^{2/3}\sin^{8/3}\left(\theta/2\right), \tag{1}$$

throughout this study. Here v, B_y, B_z, and $\theta = \tan^{-1}\left(B_y/B_z\right)$ are respectively the solar wind speed, the y and z components of the interplanetary magnetic field (IMF), and the IMF clock angle, with all quantities given in geocentric solar magnetic coordinates.

We use ϵ_N averaged over a two-hour backward-looking window, $\bar{\epsilon}_N$, as an indicator of solar wind driving. This quantity is calculated using solar wind and IMF measurements from the NASA OMNI database at one-minute resolution (King & Papitashvili, 2005).

3 Results

3.1 Conjunctions

In this section we present two conjunction events between DMSP satellites, *Swarm* satellites and the 105° magnetic meridian, on which the ground based magnetometer (GBM) electrojet boundary dataset is located.

Figure 1 shows a conjunction between the 105° magnetic meridian, the *Swarm* A and C satellites and the DMSP F17 satellite for the period between 14:33:00 and 14:53:00 on 13^{th} March 2014. Figure 2 shows a conjunction between the 105° magnetic meridian, the *Swarm* A satellite and the DMSP F18 satellite between 16:14:22 and 16:37:34 on the 22^{nd} of February 2014. In both Figures 1 and 2, the left panel shows a map illustrating the 105° meridian and the orbital trajectory of the satellites in a cubed-sphere projection during the conjunction. The top right panel shows the integrated energy flux between 1.3 and 30 keV for the electrons and ions based on measurements by the SSJ instrument onboard the DMSP satellite, together with the precipitation boundaries from Kilcommons et al. (2017). The horizontal line represents the threshold value used by Kilcommons et al. (2017). The middle right panel shows several sheet current density profiles, one for each satellite in the event. Each profile is constructed by finding the median sheet current density in S. J. Walker et al. (2023) occurring at times between when the two boundaries were identified by the particular satellite and are colour coded by the associated satellite (following the scheme in the left panel). Thus there are three median profiles in Figure 1 and two median profiles in Figure 2. The algorithm described in section 2.1.2 is applied to each median profile and the boundaries of the strongest east and west

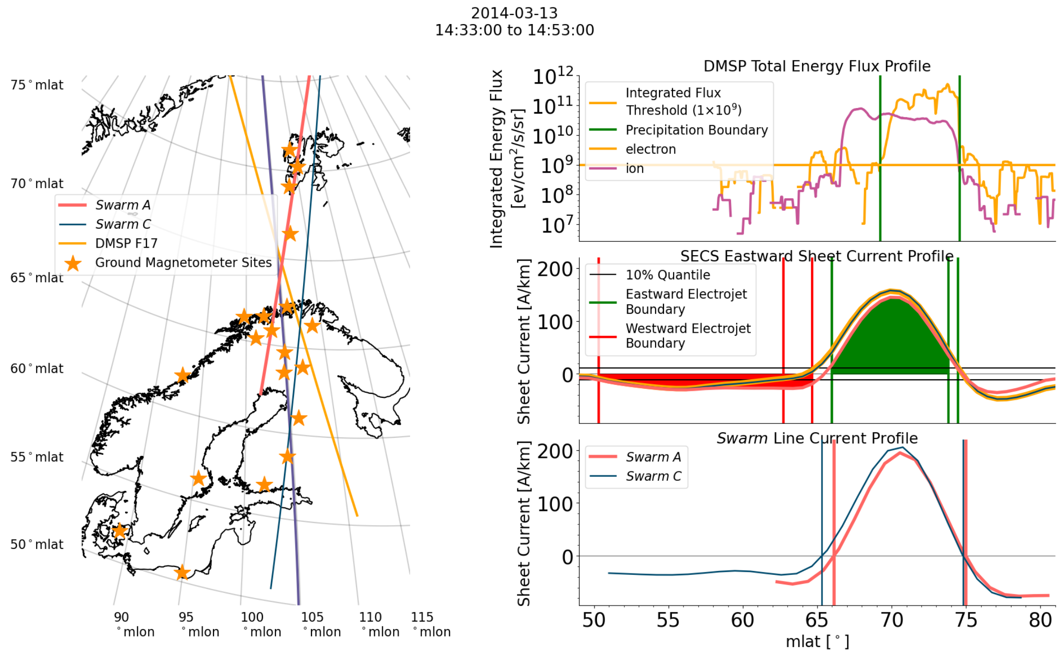

Figure 1: Conjunction event between the 105° magnetic meridian, *Swarm* A, *Swarm* C and DMSP F17, occurring between 14:33:00 and 14:53:00 UT on 13th of March 2014. The 105° magnetic meridian goes from approximately 16.5 to 16.9 MLT and $\bar{\epsilon}_N$ ranges from 3.6 to 4.3. The left panel shows a map of Fennoscandia and the location of the twenty magnetometers used by S. Walker et al. (2023), the satellite trajectories and the 105° magnetic meridian. Magnetic latitudes and longitudes are given in Apex coordinates. The top right panel shows the proton and electron energy flux measurements by DMSP F17 integrated between 1.3 and 30 keV. Vertical green lines show the auroral oval boundaries found through the method described by Kilcommons et al. (2017) and a horizontal orange line shows the associated integrated flux threshold. The middle right panel shows an application of the algorithm, described in section 2.1.2, to three median sheet current density profiles. Each median sheet current density profile is constructed by finding the median of the eastward sheet current density in S. J. Walker et al. (2022) between the time of the boundaries found using DMSP F17, *Swarm* A and *Swarm* C. The colour of each median profile indicates which satellite boundary times are used for the window to determine the median profile, following the same colour convention as the left panel. The strongest east and west current sections found using the median profile associated with *Swarm* A are highlighted with their corresponding colour. The bottom right panel shows the sheet current density profiles found using *Swarm* A and C and their associated electrojet boundaries (Viljanen et al., 2020; Kervalishvili et al., 2020). The colour of the profiles and corresponding boundaries are the same colour to identify the satellite used.

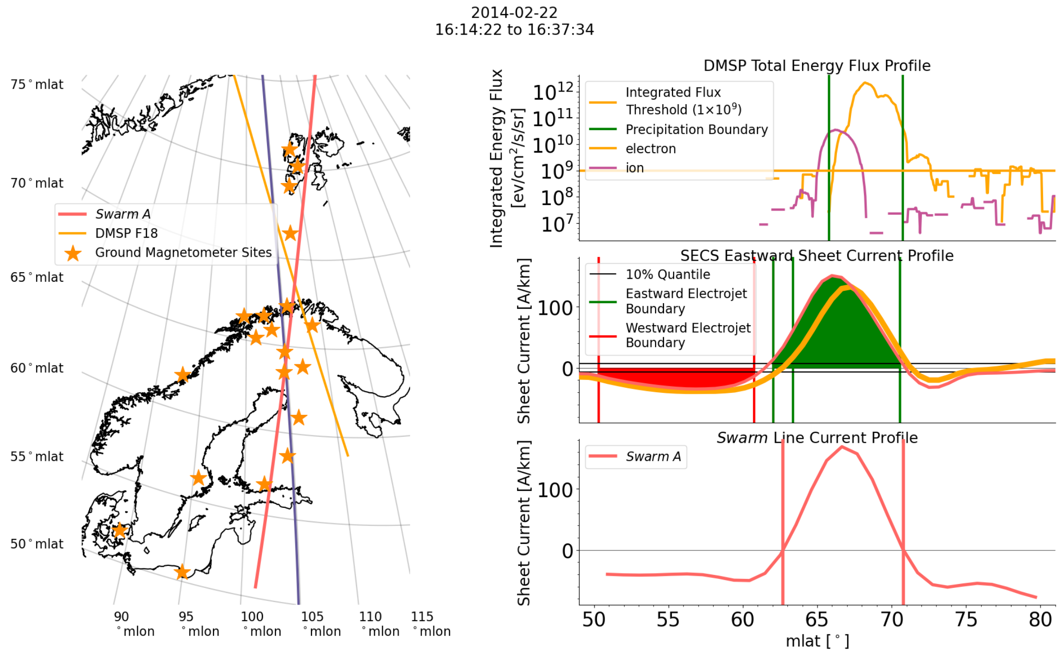

Figure 2: Conjunction event between the 105° magnetic meridian, *Swarm* A and DMSP F18, occurring between 16:14:22 and 16:37:34 UT on 22^{nd} of February 2014, in the same format as Figure 1. The 105° magnetic meridian goes from approximately 18.2 to 18.6 MLT and $\bar{\epsilon}_N$ has a range of 5.4 to 6.1.

current for each median profile are shown with green and red vertical lines respectively. The 10% quantile, which is used for the boundary first guess (cf. section 2.1.2), is shown and the strongest east and west currents are highlighted with their corresponding colours for the median profile associated with the *Swarm* A conjunction in Figure 1 and 2. The bottom right panel shows the sheet current density profiles, derived using the line current method and the *Swarm* magnetometers, and the boundaries of the eastward current (Aakjær et al., 2016; Viljanen et al., 2020; Kervalishvili et al., 2020).

In both conjunctions we find a clear similarity between the SECS derived eastward current, based on ground magnetometers, and the line current derived eastward currents, based on *Swarm* magnetometers. Unsurprisingly, we also see that the boundaries from the two electrojet datasets are very similar particularly if one considers the separation of the data points for the GBM electrojet boundaries, approximately 0.65° MLat. In both conjunctions we find the DMSP poleward boundary to coincide with the poleward electrojet boundaries, but the equatorward boundary is situated close to the peak of the electrojet. The equatorward extent of the integrated ion flux above the threshold matches well with the equatorward boundary of the electrojet, but the poleward extent only matches with the poleward boundary of the electrojet in Figure 1. Despite the short time scale of the conjunctions, the electrojet is not constant. In Figure 1 there is approximately ten minutes separation between the boundaries produced by *Swarm* A and C. Both the associated median GBM current and *Swarm* based magnetometer (SBM) current show clear differences, but the GBM and SBM poleward boundaries are relatively stable over this time period. However, the *Swarm* C and DMSP F17 boundaries are approximately two minutes apart which is why they have near identical median GBM current profiles and the boundaries found from these current profiles are identical. In Figure 2 the *Swarm* A and DMSP F18 boundaries are approximately 10 minutes apart which may contribute

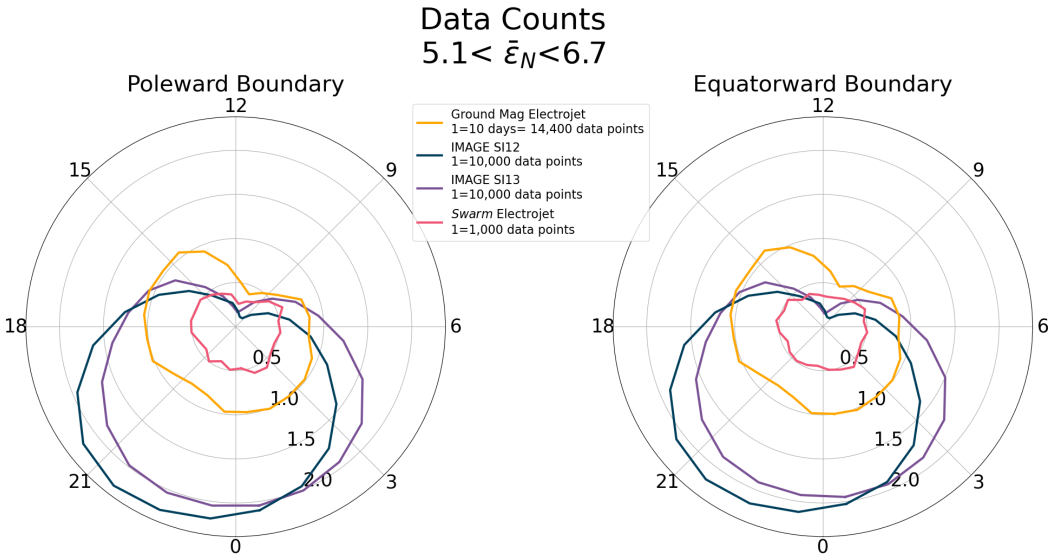

Figure 3: Data coverage and distribution of the SI12, SI13, SBM electrojet and GBM electrojet boundaries from one $\bar{\epsilon}_N$ bin, from Figure 5 and 6, and using the same MLT binning as used in Figure 5 and 6. The left panel shows the data distribution for the poleward boundary and the right panel shows the data distribution for the equatorward boundary.

to significantly different median GBM current profiles and clear differences in the equatorward GBM boundary. But, once again, the poleward boundary shows stability over this period and is identical for the median GBM current profiles associated with DMSP F18 and *Swarm* A.

3.2 Data Availability and Distribution

In the following section we present and describe a statistical investigation of the various boundary datasets.

Six bins of close to equal sample size have been created using $\bar{\epsilon}_N$ for the ground based magnetometer electrojet boundary dataset. These bins are applied to all the datasets and additionally binned by MLT bins of size 1 h starting at 0–1 MLT. The mean Newell epsilon values and binning are explained further in section 3.3. Figure 3 shows the number of poleward and equatorward boundaries that contribute to the $5.1 < \bar{\epsilon}_N < 6.7$ bin for all datasets. The general MLT trend and relative difference between the data sets is not greatly different between the different $\bar{\epsilon}_N$ bins used in Figures 5 and 6. There are much fewer SBM boundaries compared to other datasets and all four datasets show a reduction in the number boundaries pre-noon, however this reduction is much more significant with the FUV boundaries. The difference in the counts between the poleward and equatorward boundaries is minimal for all datasets. There is also a reduction in the number of GBM boundaries between 20 and 23 MLT and, although we do not show these plots, a similar behaviour can be observed for weaker $\bar{\epsilon}_N$ for the SBM boundaries.

Figure 4 shows the median absolute deviation (MAD) of the poleward and equatorward boundaries, as the radial value (in degrees), for the same $\bar{\epsilon}_N$ range as used in Figure 3, in order to depict the spread of the distribution behind each statistic. In general, including the bins not shown, the MAD of the poleward and equatorward boundary for the electrojet boundaries are very similar, particularly in terms of the location

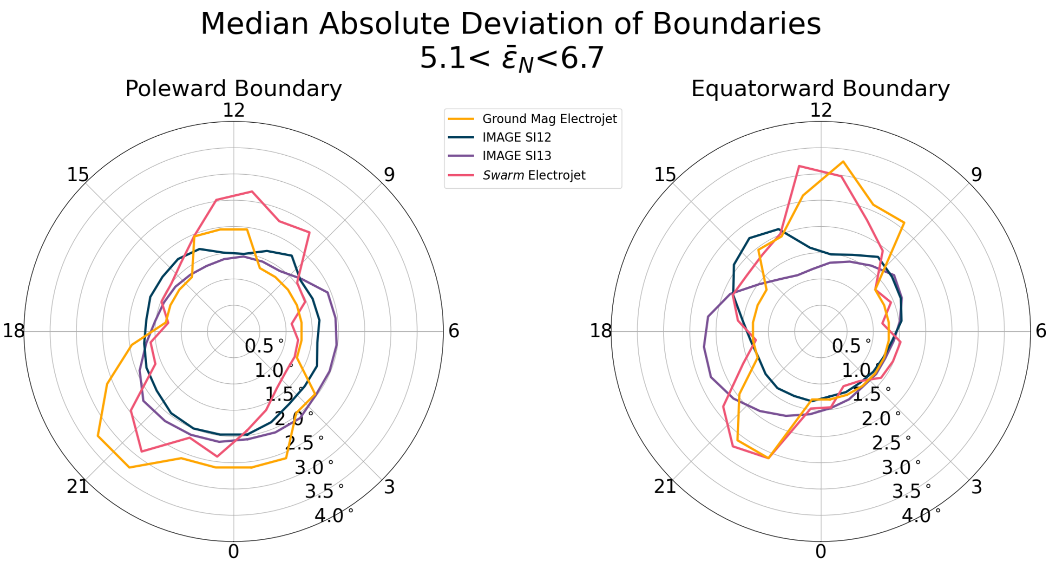

Figure 4: Same as Figure 3 but the median absolute deviation (MAD) is calculated instead of the data counts in each MLT bin.

of the peaks. The same cannot be said for the MAD of the SI12 and SI13 boundaries which exhibit peaks at 15 and 18 MLT respectively for the equatorward boundary but no clear peaks for the poleward boundary. Furthermore, the peaks in the MAD of the poleward boundary and equatorward boundary for all datasets is consistent across all bins of $\bar{\epsilon}_N$. Overall the FUV boundaries have a smaller MAD than the other datasets, most significantly where the MAD peaks in GBM and SBM boundaries between 9 and 12 MLT and 20 and 23 MLT. However the MAD of the equatorward boundaries is comparable between 14 and 18 MLT and between 3 and 9 MLT and where the MAD of the FUV poleward boundaries peak their MAD is the largest of the datasets.

3.3 The dependence of average boundaries on solar wind coupling

We now present and describe the statistical maps (median values) of the different boundary datasets introduced in section 2.

Figure 5 shows the median equatorward and poleward auroral boundaries using the SI12 and SI13 imagers on IMAGE (Chisham et al., 2022) as blue and purple lines respectively, together with the median ground based magnetometer (GBM) electrojet boundaries (this study) shown with orange lines. The auroral occurrence probability based on the SSJ instrument onboard the DMSP satellites (Kilcommons et al., 2017; Decotte et al., 2023) is shown in grey-scale. Each plot within the figure represents a different $\bar{\epsilon}_N$ bin, reflecting its value averaged over the two hours prior to the boundary detection. The limits have been chosen so that the number of GBM electrojet boundaries is similar in each bin. Six bins have been created but the final bin ($\epsilon_N > 9.1$) is omitted due to its large range and having comparatively more anomalous data. The IMAGE boundaries are selected when there are at least four boundaries available for an image, to avoid spurious boundaries. In addition to the algorithm described in section 2.1.2, the electrojet boundaries in Figure 5 are further screened to ensure confidence in the boundaries we present: (1) For each minute of data in S. J. Walker et al. (2022) the electrojet boundaries are defined as the boundaries identified for the strongest current section (where strength is defined as the absolute total current of the section). (2) The boundaries of the elec-

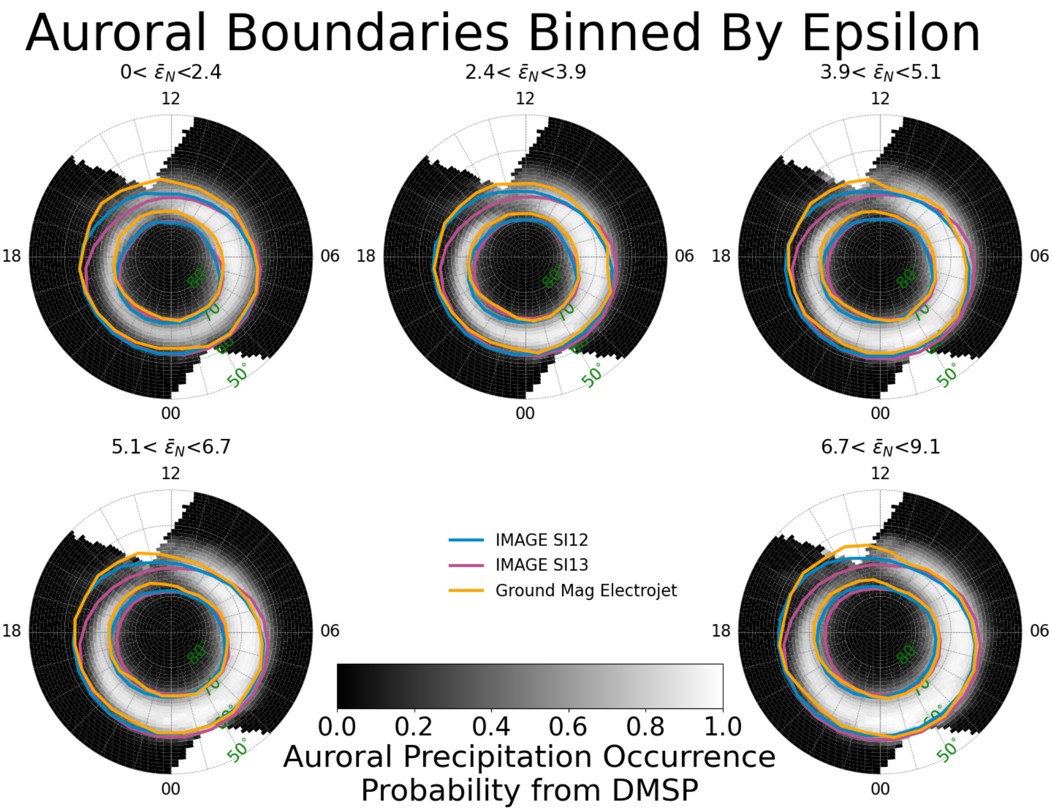

Figure 5: Median SI12, SI13 and GBM electrojet boundaries in 5 bins of $\bar{\epsilon}_N$ (see section 2.6) and in 24 MLT bins of size 1 h, with the first bin being 0-1 MLT. The background colour is used to show the auroral precipitation occurrence probability found by Decotte et al. (2023) and using their spatial bins and additionally binned by our $\bar{\epsilon}_N$ ranges.

trojet are checked for their proximity to the edge of the meridian, those occurring on the first three data points of the meridian (less than 50.5° MLat) and the last three data points (greater than 79.5° MLat) are removed to ensure that the boundary of the electrojet can be seen in S. J. Walker et al. (2022). (3) When an eastward electrojet is chosen the peak must be larger than 0.05 A/km and for a westward electrojet the peak must be below -0.1 A/km. (4) Finally, to make the boundaries comparable to those produced by Chisham et al. (2022) we bin the electrojet boundaries using MLT bins of width 1 MLT, centred at half MLTs. Additionally, we have used used bootstrapping to calculate how well defined the median of the datasets are. This is done using the scipy bootstrap function (Virtanen et al., 2020) where the use of default values creates 9999 random realisations of the data (all the data that contributes to one median data point in Figure 5) each the same size as the initial data. The median is then found for each realisation producing 9999 realisations of the median and then the standard deviation is calculated using these medians which we refer to as the bootstrapped standard deviation of the median from hereafter. We do not show the bootstrapped standard deviation of the median as the values are small. SBM has the largest bootstrapped standard deviations of all the dataset but, even so, the values do not exceed half a degree and therefore the medians of each dataset can be considered well defined. However this should not be considered an indication of the spread of the distributions of the datasets, which is quantified by the MAD values in Figure 4, and further explored in section 4.

We see a remarkable similarity between the SI12 boundaries and the electrojet boundaries in most MLT sectors, however, differences are apparent in the pre-midnight sector and around 15 MLT. In general for both boundaries SI12 is closer to the electrojets in comparison to the auroral occurrence probability and SI13. As $\bar{\epsilon}_N$ increases the SI12 and electrojet boundaries on the dayside become closer but in the pre-midnight sector they become further apart, in this sector the SI12 boundaries remain quasi circular but the GBM boundaries increasingly deviate towards a straight line as $\bar{\epsilon}_N$ increases.

Figure 6 shows median boundaries for the GBM electrojets and the *Swarm* based magnetometer (SBM) electrojets, as purple and orange lines respectively, using the same MLT and $\bar{\epsilon}_N$ bins as in Figure 5. The same auroral occurrence probability maps are also shown. The FAC boundary model (Xiong & Lühr, 2014) is shown as a blue dashed line, where the midpoint of the $\bar{\epsilon}_N$ bin is used as input for the model. As stated previously the bootstrapped standard deviation of the datasets presented are small and thus the median boundaries in Figure 6 are well defined.

The different electrojet boundary datasets show a significant similarity for most MLT and $\bar{\epsilon}_N$ bins but the largest deviations appear on the night side for the poleward boundary and increase with $\bar{\epsilon}_N$. The equatorward boundary of the FAC boundary model shows similarities with the electrojet boundary datasets, however much like FUV boundaries in Figure 5 the FAC and electrojet boundaries are a poorer match in the pre-midnight sector where the shape of the electrojet boundaries change. In general the comparison is much worse between the FAC model and the electrojet boundaries for weaker $\bar{\epsilon}_N$, even more so for the poleward boundary than the equatorward boundary.

3.4 Seasonal variability of median boundaries

Using satellite based FUV images and measurements of particle precipitation, previous studies have investigated how season affects the auroral oval (Oznovich et al., 1993), the OCB (Laundal et al., 2010), and the equatorward boundary of the diffuse aurora (Landry & Anderson, 2019). In this section we investigate how the different boundary datasets used in this study vary with season, with summer and winter defined respectively as when the dipole tilt is $\psi > 10°$ and $\psi < -10°$, since we only use data from the Northern hemisphere.

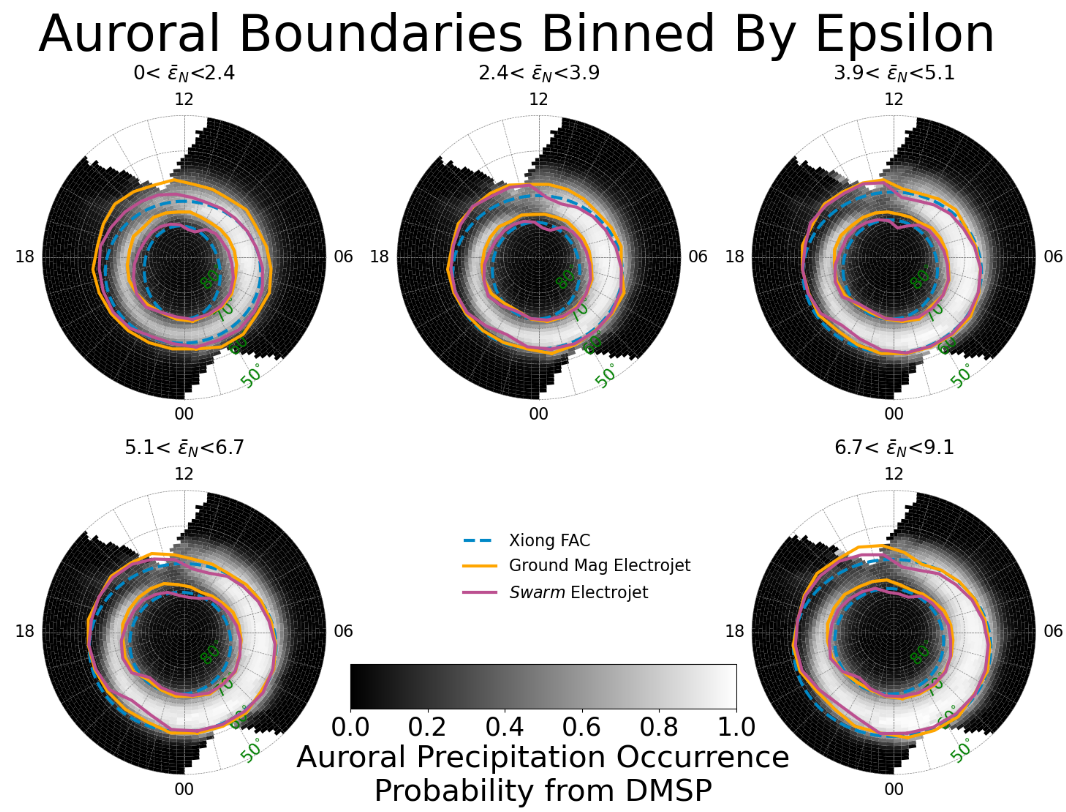

Figure 6: Constructed the same as Figure 5 but using SBM electrojet boundaries instead of SI12 and SI13. Additionally, FAC boundaries are found for each $\bar{\epsilon}_N$ bin by using the midpoint of the bins as input for the model (Xiong & Lühr, 2014).

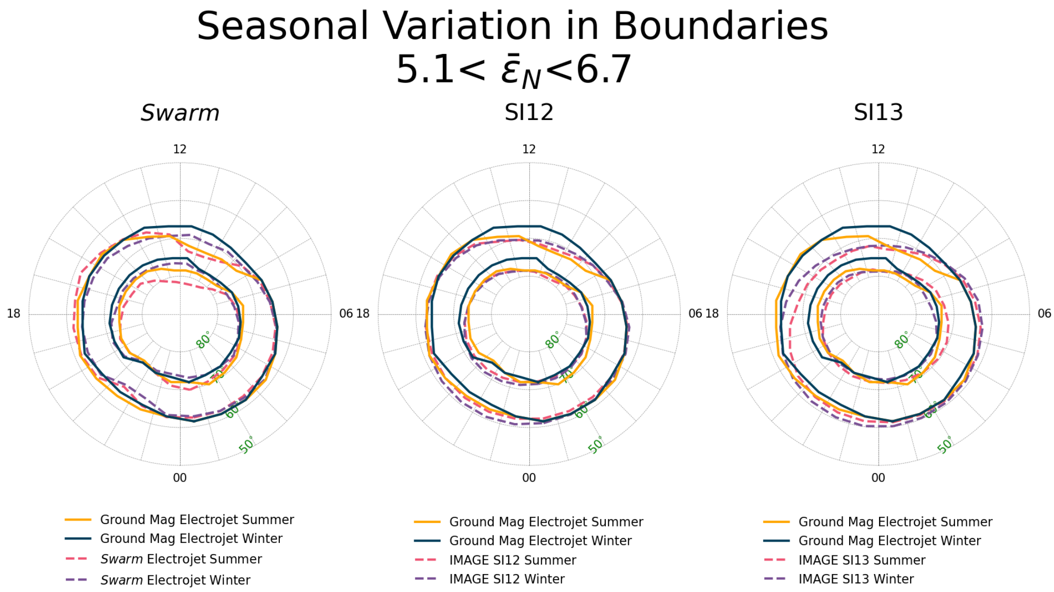

Figure 7: Median SI12, SI13, SBM electrojet boundaries compared with the GBM electrojet boundaries within one $\bar{\epsilon}_N$ bin from Figure 5 and 6 and using the same MLT bins. Boundaries are additionally binned into summer and winter, where summer is defined as when the dipole tilt is greater than 10° and winter is defined as when the dipole tilt is less than -10°. The left panel compares the seasonally binned GBM and SBM electrojet boundaries. The middle panel compares the seasonally binned GBM electrojet boundaries and the SI12 boundaries. The right panel compares the seasonally binned GBM electrojet boundaries and the SI13 boundaries.

Figure 7 shows the median of the poleward and equatorward boundary for each boundary dataset, using the same MLT binning used in Figure 5 and the $5.1 < \bar{\epsilon}_N < 6.7$ bin from the same Figure. From left to right the panel compares seasonal GBM electrojet boundaries with SBM electrojet boundaries, SI12 boundaries and SI13 boundaries respectively, where winter is defined as when the dipole tilt is less than $-10°$ and summer when the dipole tilt is greater than $10°$. We have also calculated the bootstrapped standard deviation for the median boundaries shown, finding that they are typically less than $0.6°$ across all datasets for both summer and winter and the poleward and equatorward boundaries. Once again the SBM boundaries have the largest bootstrapped standard deviation but even the larger spikes do not exceed one degree. Since the GBM dataset is from a fixed geographic location, it has its own inherent dipole tilt relation for a given MLT location, leading to systematic dipole tilt variations in MLT within the allowed summer/winter range. Additionally there exist biases within the distribution of each magnetometer's availability per month that can shift the median month in summer and winter away from the solstices. Hence, subtle seasonal differences should be interpreted with care. The GBM equatorward boundary shows little difference due to season at dawn and from 14 to 17 MLT. However, significant differences can be seen from 8 to 14 MLT and pre-midnight. The GBM poleward boundary shows seasonal differences at all MLT sectors, being closest around 5 MLT and most different around 17 MLT.

In the left panel we can see how the GBM and SBM boundaries compare seasonally. The SBM equatorward and poleward boundaries are similarly affected by season as the GBM boundaries are, in particular we see around 5 MLT that even the different datasets show little difference for both the poleward and equatorward boundaries. In other sectors the datasets are not as good a match. However, the seasonal trend is much the same, where the electrojet is more poleward during the summer in the pre-noon sector and more equatorward from 18 to 24 MLT. The pre-noon sector shows a clear shift in the equatorward boundary of the electrojet during the summer, deviating from the more circular path that is visible during the winter. There is a similar behaviour for the SBM poleward boundaries but not so clearly for the GBM poleward boundaries, an effect that could be attributed to the latitudinal limit of the datasets as the median poeward boundary for the SBM dataset is beyond the latitudinal extent of the GBM dataset.

In the middle panel there is minimal seasonal variation in the SI12 poleward and equatorward boundaries. Therefore, although during summer the SI12 boundaries are similar to the GBM boundaries, in the winter they are not. The biggest difference between the SI12 and GBM equatorward boundaries occurs pre-noon and pre-midnight in both seasons. For the poleward boundary the biggest difference occurs between 11 and 20 MLT during the winter and 13 to 20 MLT in the summer.

In the right panel we see that SI13 has a greater seasonal variation in both boundaries than for SI12. For the equatorward boundary the greatest seasonal variation occurs from noon to midnight but from midnight to noon for the poleward boundary. Although the GBM boundaries do not match as well with SI13 as they do with SI12, there are some MLT sectors where the seasonal trends agree. In the SI12 and 13 datasets in the summer the equatorward boundary pre-noon exhibits a poleward shift and the poleward boundary has a poleward shift from 13 to 21 MLT and an equatorward shift between 1 and 6 MLT.

4 Discussion

Knowledge of the location of auroral oval boundaries is an important tool for understanding space weather and solar wind - magnetosphere coupling (Chisham et al., 2008). In particular, knowledge of the location of the OCB is very useful (Chisham, 2017), and a global and continually available proxy of the OCB would be invaluable. There are challenges associated with finding these boundaries through more conventional measurements such as auroral images and particle precipitation measurements. Here, we have proposed the advantages of understanding the auroral oval through the auroral electrojets due to the temporal and spatial prevalence of ground based magnetometers. In this section we discuss the results presented in section 3, with a focus on how our electrojet boundary dataset compares both statistically and in case studies to *Swarm*-based magnetometer electrojet boundaries (Kervalishvili et al., 2020; Viljanen et al., 2020) and other common means of estimating the auroral oval (SI12, SI13 and auroral precipitation occurrence probability) (Chisham et al., 2022; Decotte et al., 2023; Kilcommons et al., 2017).

In Figure 6 we presented the modelled FAC boundaries (Xiong & Lühr, 2014) together with the median electrojet boundary and auroral occurrence probability maps. One must be careful when interpreting differences between the FAC boundary model, the median boundaries and auroral occurrence probability because the $\bar{\epsilon}_N$ used to constrain the model and the $\bar{\epsilon}_N$ used to bin the boundary data are calculated through different methods (Xiong & Lühr, 2014). Despite this, the trend of increasing eccentricity of the poleward and equatorward boundaries as $\bar{\epsilon}_N$ weakens remains a valid similarity between the FAC boundaries and the SBM and GBM electrojet boundaries. Due to the latitude limit of the GBM electrojet boundaries the increase in eccentricity is clearer for the SBM electrojet poleward boundary than the GBM electrojet poleward boundary. Excluding regions affected by the pre-noon and pre-midnight electrojet discontinuities, it is likely that an ellipse would represent an appropriate geometry for an electrojet boundary model and a similar approach to Xiong and Lühr (2014) could be a fruitful endeavour.

The SBM and GBM electrojet boundaries are similar both statistically (Figure 6) and in the two conjunction studies we present in section 3.1 (Figure 1 and 2). However, at the electrojet discontinuities, around pre-midnight and pre-noon (regions surrounding and including the location of convection reversal), the SBM and GBM electrojet are dissimilar from each other and from the SI12 and SI13 boundary datasets. It is in these regions that we also observe spikes in the MAD of both boundaries from the SBM and GBM datasets (Figure 4), and a dip in the counts (Figure 3). Johnsen (2013) comments on the challenges of determining the electrojet boundaries at these discontinuities due to the elevated complexity of the current systems, and omits these regions from their boundary determination using three- and four-hour universal time (UT) windows for the pre-noon and pre-midnight discontinuities, respectively. However, we see in Figure 5 that on average the electrojet boundaries deviate more from the auroral oval (as defined by SI12) with increasing $\bar{\epsilon}_N$ value and with a greater range of MLTs affected. This suggests that a fixed window is not suitable and that in many cases useful information about the boundaries is likely discarded.

To understand how different boundary datasets are affected in the discontinuity regions, we present in Figure 8 the distribution of the boundaries in two MLT bins around magnetic noon (11–12 MLT and 12–13 MLT) and two MLT bins around pre-midnight (20–21 and 21–22 MLT) for a single $\bar{\epsilon}_N$ bin (5.1–6.7) from Figure 5. There are two peaks in the distribution of GBM and SBM electrojet boundaries, most prominent in the distribution of poleward boundaries, which suggests two distinct populations. Equivalent current maps in S. Walker et al. (2023) show that either side of the discontinuities the strongest current sections are opposite in direction. Consequently, our algorithm will describe the auroral oval using the boundaries of the strongest eastward current section in the afternoon and dusk sectors and using the boundaries of the strongest westward current section in the dawn and morning sectors. In the Harang Discontinuity (HD) a low latitude strong westward (eastward) current flows into a high latitude westward (eastward) current as the discontinuity is traversed clockwise (anti-clockwise) and the opposite is the case for the dayside discontinuity. While in the other MLT sectors the low latitude current section is on average much stronger than the high latitude current section, the strengths become more similar the closer we get to the discontinuities. In our bound-

$5.1 < \bar{\epsilon}_N < 6.7$

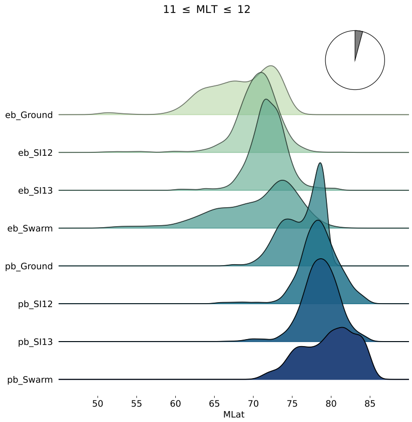

(a) Boundary distributions between 11 and 12 MLT

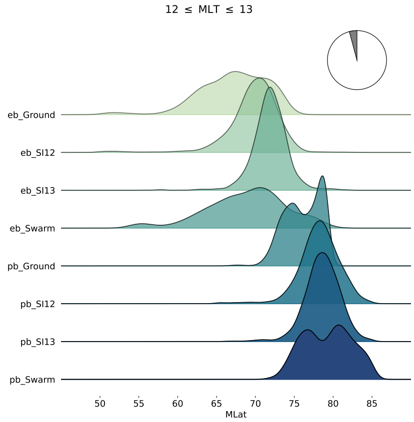

(b) Boundary distributions between 12 and 13 MLT

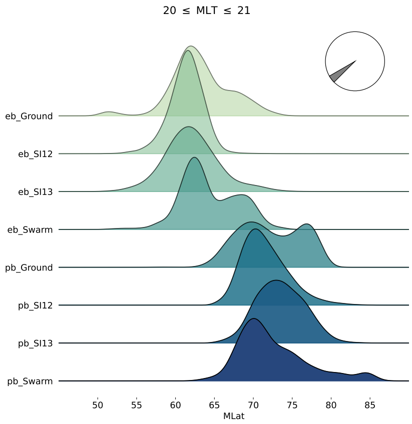

(c) Boundary distributions between 20 and 21 MLT

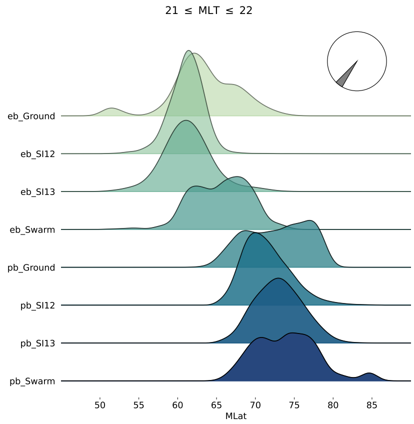

(d) Boundary distributions between 21 and 22 MLT

Figure 8: Distribution of the poleward boundary and equatorward boundary for the SI12, SI3, SBM electrojet and GBM electrojet boundary datasets within one $\bar{\epsilon}_N$ bin from Figure 5 and 6. Four MLT bins are selected from Figure 5 and 6, 11 to 12 MLT (a), 12 to 13 MLT (b), 20 to 21 MLT (c) and 21 to 22 MLT (d).

aries we observe this as the boundary distributions becoming more bimodal and the average shifting poleward as we come closer to the average location of the discontinuities due to the increase in probability of selecting the high latitude current section.

Given that ambiguity in the dominant current section causes a poleward shift in the average boundaries we can use the poleward shift in the GBM and SBM electrojet boundaries in Figure 5 and 6 to identify where and how often the ambiguity occurs. SBM exhibits a greater poleward shift than the GBM dataset and this is due to the latitude limitations of the GBM data set, a consequence of the latitude distribution of magnetometers in Fennoscandia (S. Walker et al., 2023). We also see in Figure 6 that the ambiguity pre-midnight covers a greater range of MLTs than pre-noon, something that can be the result of a difference in the size of the HD and the dayside discontinuity or/and a difference in the distribution in the MLT location of the two discontinuities. The MLT distribution of the discontinuity on the dayside is expected to depend on the IMF B_y, which strongly controls the plasma flow resulting from dayside reconnection (e.g., Laundal et al., 2018). Further separation by IMF B_y could shed light on the effect of B_y on the GBM/SBM poleward boundary variation. As we can see in Figure 7, the poleward shift in the boundaries at the dayside electrojet discontinuity is enhanced during the summer compared to the winter. However, there appears to be no significant seasonal variation in the effect in the HD region. This difference in seasonal variation between the dayside and the nightside could be an effect of corresponding variations in solar EUV produced conductance, which is more important on the dayside. In terms of the use of the GBM and SBM electrojet boundary datasets as auroral oval proxies one must consider the proximity to the HD and dayside discontinuity, solar wind driving ($\bar{\epsilon}_N$) and dipole tilt in order to determine the likelihood of dominant current section ambiguity.

When analysing Figure 5 we find that the GBM electrojet boundaries, in most MLT sectors, are as close to the SI12 boundaries as they are to the SBM electrojet boundaries, particularly as $\bar{\epsilon}_N$ increases. On the other hand, the SI13 boundaries are only close when the differences between SI12 and SI13 are small. Feldstein et al. (1999) found that the eastward electrojet often extends equatorward of the auroral oval as defined by electron precipitation; this is the same relationship that we observe between the electrojet boundaries and the SI13 boundaries and the auroral occurrence probability. Given that SI12 measures the emissions related to proton precipitation and SI13 measurements are dominated by emissions related to electron precipitation (Coumans et al., 2004; Gérard et al., 2001; Frey et al., 2001), our results and the results of Feldstein et al. (1999) therefore support one another, and contradict the notion that the electrojets must flow within the auroral oval as defined by electron precipitation (Rostoker et al., 1996).

Although SI13 is related to the precipitation of auroral energy electrons, Figure 5 shows that the auroral precipitation occurrence probability maps do not everywhere align well with the SI13 boundaries, in particular in the pre-noon sector where the auroral precipitation occurrence probability extends far equatorward of all the boundary datasets in this study. In general the SI13 boundaries and the auroral precipitation occurrence probability become more dissimilar for weaker $\bar{\epsilon}_N$ values but the opposite is the case in the pre-noon sector. Figure 1 and 2 occur in the MLT ranges 16.5–16.9 and 18.2–18.6 and with $\bar{\epsilon}_N$ ranges of approximately 3.6–4.3 and 5.4–6.1, respectively.

Although Feldstein et al. (1999) do not examine the latitude limits of auroral energy proton precipitation they do comment on the peak in proton precipitation occurring close to the centre of the eastward electrojet. Similarly, in Figure 1 and 2 we find the centre of enhanced auroral energy proton precipitation occurs around the centre of the eastward electrojet. Both in the median boundaries (Figure 5) and in the first conjunction (Figure 1) we observe an extension of the relationship between the eastward electrojet and proton precipitation, where limits of the precipitation are close to or coincident with the eastward electrojet boundaries. Figure 1 and 2 show the same as Feldstein et al. (1999) and the median boundaries, that the eastward electrojet can extend equatorward of the electron precipitation defined auroral oval. However, the poleward limit of the electron precipitation occurring close to the poleward boundary of the eastward electrojet that can be see in Figures 1 and 2 is not shown in Figure 5 or in Feldstein et al. (1999) but is seen for the westward electrojet in Figure 5 and Feldstein et al. (1999). Finally, in Figure 2 the latitudinal extent of the proton precipitation poorly reflects the electrojet boundaries. Despite this, the equatorward boundary of the proton precipitation is much closer to the electrojet boundary than for the electron precipitation. Feldstein et al. (1999) finds a large variation in the relationship between precipitation regions and boundaries and the electrojet boundaries and centres, something that is also clear in this study with the difference between patterns in the average boundaries (Figure 5), and the direct comparisons (Figure 1 and 2). A greater number of direct comparisons may be required to ensure the trends in the average boundaries are representative of the trends in reality. In summation, with the results presented one must be careful when interpreting the auroral oval boundaries derived from the electrojet boundaries based on what is seen in the trends of the average boundaries.

5 Conclusion

Finding the boundaries of the auroral oval is of key importance in understanding the region of enhanced space weather hazards in the polar regions. In particular the OCB allows us to quantify the amount of open flux in the polar cap and subsequently understand the amount of energy stored in the magnetotail. In this study we have developed an algorithm that, among other properties, detects the boundaries of the auroral electrojets. Taking advantage of the eastward sheet current density profiles produced by S. Walker et al. (2023), we have created a dataset through the use of our algorithm that spans twenty years and, due to data gaps, totals eleven years with minute cadence. We make this dataset publicly available due to the large range of applications that go beyond the scope of this paper.

The goal of our study was to understand the feasibility of an auroral oval boundary proxy based on our electrojet boundaries. We have found that the auroral oval described through proton and electron precipitation, and their associated FUV aurora, can be variable. Even the comparison between the median boundaries from SI13 images and electron precipitation measurement-based auroral occurrence probability can be significantly variable. As such the relationship between the electron precipitation auroral oval and the electrojet boundaries and the relationship between the proton precipitation auroral oval and electrojet boundaries is very different. We find the proton precipitation auroral oval boundaries are much more coincident with the electrojet boundaries. Consequently, we find that the electrojets can flow outside the electron precipitation auroral oval which agrees with Feldstein et al. (1999) but, as the auroral oval is more typically described by electron precipitation (Kilcommons et al., 2017; Newell et al., 1996; Feldstein & Starkov, 1967), this is contrary to the general description of the ionosphere.

If we move to the paradigm of describing the auroral oval through proton precipitation we can see that there is indeed on average a close resemblance between the auroral oval and the electrojet boundaries. However, determination of the auroral oval from the electrojet boundaries encounters three key challenges: (1) Increasing dominant current section ambiguity with proximity to the electrojet discontinuities makes electrojet boundaries in the pre-noon and pre-midnight sectors a very poor proxy of the auroral oval. (2) The similarities between the electrojet boundaries and the auroral oval boundaries show a seasonal and reconnection rate ($\bar{\epsilon}_N$ value) dependence. (3) While the auroral oval and electrojet boundaries are statistically similar, analysis of conjunctions shows that even under favourable conditions and locations the truth does not always match the average.

Finally, while we are not the first to find the electrojet boundaries on a routine basis (Johnsen, 2013; Viljanen et al., 2020), we are the first to provide a publicly available dataset that is based on ground magnetometers with a significant temporal advantage over those produced from measurements by the *Swarm* satellites. The global shape of the electrojet and its relationship with the auroral oval shows to be an important property of polar ionospheric dynamics and simply reducing the electrojet to singular values, such as the AL and AU indices, will significantly hinder understanding of this field (Kamide & Akasofu, 1983; Rostoker et al., 1980) and limit the capabilities of interpreting the auroral oval when global FUV images are not available or are ineffective.

6 Data Availability Statement

The solar wind and interplanetary magnetic field measurements has been downloaded from the OMNI database: `https://cdaweb.gsfc.nasa.gov/sp_phys/data/omni/hro_1min/`. The dataset of electrojet boundaries and properties can be found at (S. J. Walker et al., 2023). The BAS-derived IMAGE auroral boundaries can be found at https://doi.org/10.5285/fa592594-93e0-4ee1-8268-b031ce21c3ca (Chisham, 2022). The dataset of *Swarm* derived electrojet boundaries can be found through `https://vires.services/` (Viljanen et al., 2020).

7 Open Research

Acknowledgments

This work was supported by Research Council of Norway under contracts 223252/F50 and 300844/ F50 and by the Trond Mohn Foundation.

GC was supported by the British Antarctic Survey Polar Science for a Sustainable Planet Programme, funded by the UK Natural Environment Research Council (NERC) as well as the UK NERC directed grant NE/V002732/1.

The authors would like to thank those involved in producing the IMAGE boundary data sets: Peter Boakes, Nicola Longden, Angeline Burrell, Mervyn Freeman, Steve Milan, and Gary Abel.

The original raw IMAGE FUV data were provided courtesy of the instrument PI Stephen Mende (University of California, Berkeley). We thank the PI, the IMAGE mission, and the IMAGE FUV team for data usage and processing tools. The raw image data, and software, were acquired from http://sprg.ssl.berkeley.edu/image/.

We extend our gratitude to the members of the International Space Science Institute (ISSI) International Team project #506 Understanding Mesoscale Ionospheric Electrodynamics Using Regional Data Assimilation for the discussions and insight into the topic of study. We also thank ISSI Bern for hosting the team.

References

Aakjær, C. D., Olsen, N., & Finlay, C. C. (2016, 8). Determining polar ionospheric electrojet currents from Swarm satellite constellation magnetic data. *Earth, Planets and Space*, *68*(1), 1–14. Retrieved from `https://earth-planets-space.springeropen.com/articles/10.1186/s40623-016-0509-y` doi: 10.1186/s40623-016-0509-y

Amm, O. (1997, 7). *Ionospheric Elementary Current Systems in Spherical Coordinates and Their Application* (Vol. 49; Tech. Rep. No. 7). Retrieved from `http://joi.jlc.jst.go.jp/JST.Journalarchive/jgg1949/49.947?from=CrossRef` doi: 10.5636/jgg.49.947

Amm, O., & Viljanen, A. (1999). Ionospheric disturbance magnetic field continuation from the ground to the ionosphere using spherical elementary current systems. *Earth, Planets and Space*, *51*(6), 431–440. doi: 10.1186/BF03352247

Andersson, L., Peterson, W. K., & McBryde, K. M. (2004, 8). Dynamic coordinates for auroral ion outflow. *Journal of Geophysical Research: Space Physics*, *109*(A8), 8201. Retrieved from `https://onlinelibrary.wiley.com/doi/full/10.1029/2004JA010424https://onlinelibrary.wiley.com/doi/abs/10.1029/2004JA010424https://agupubs.onlinelibrary.wiley.com/doi/10.1029/2004JA010424` doi: 10.1029/2004JA010424

Boakes, P. D., Milan, S. E., Abel, G. A., Freeman, M. P., Chisham, G., Hubert, B., & Sotirelis, T. (2008, 9). On the use of IMAGE FUV for estimating the latitude of the open/closed magnetic field line boundary in the ionosphere. *Annales Geophysicae*, *26*(9), 2759–2769. Retrieved from `www.ann-geophys.net/26/2759/2008/` doi: 10.5194/angeo-26-2759-2008

Bothmer, V., Bothmer, & Volker. (2013). AFFECTS - Advanced Forecast For Ensuring Communications Through Space. *EGUGA*, *15*, 2013–11752. Retrieved from `https://ui.adsabs.harvard.edu/abs/2013EGUGA..1511752B/abstract`

Burrell, A. G., Chisham, G., Milan, S. E., Kilcommons, L., Chen, Y. J., Thomas, E. G., & Anderson, B. (2020, 4). AMPERE polar cap boundaries. *Annales Geophysicae*, *38*(2), 481–490. doi: 10.5194/angeo-38-481-2020

Carbary, J. F. (2005, 10). A Kp-based model of auroral boundaries. *Space Weather*, *3*(10), n/a-n/a. Retrieved from `https://onlinelibrary.wiley.com/doi/full/10.1029/2005SW000162` doi: 10.1029/2005SW000162

Chisham, G. (2017, 1). A new methodology for the development of high-latitude ionospheric climatologies and empirical models. *Journal of Geophysical Research: Space Physics*, *122*(1), 932–947. Retrieved from `https://onlinelibrary.wiley.com/doi/full/10.1002/2016JA023235` doi: 10.1002/2016JA023235

Chisham, G. (2022). *Ionospheric boundaries derived from IMAGE satellite mission data (May 2000 - October 2002) - VERSION 2.0 (Version 2.0) [Data set].*

Chisham, G., Burrell, A. G., Thomas, E. G., & Chen, Y. J. (2022, 7). Ionospheric Boundaries Derived From Auroral Images. *Journal of Geophysical Research: Space Physics*, *127*(7). doi: 10.1029/2022JA030622

Chisham, G., Freeman, M. P., Abel, G. A., Lam, M. M., Pinnock, M., Coleman, I. J., ... Villain, J. P. (2008, 3). Remote sensing of the spatial and temporal structure of magnetopause and magnetotail reconnection from the ionosphere. *Reviews of Geophysics*, *46*(1). Retrieved from `https://onlinelibrary.wiley.com/doi/full/10.1029/2007RG000223` doi: 10.1029/2007RG000223

Coumans, V., Gérard, J. C., Hubert, B., Meurant, M., & Mende, S. B. (2004, 4). Global auroral conductance distribution due to electron and proton precipitation from IMAGE-FUV observations. *Annales Geophysicae*, *22*(5), 1595–1611. doi: 10.5194/ANGEO-22-1595-2004

Decotte, M., Laundal, K. M., Hatch, S. M., & Reistad, J. P. (2023, 6). Auroral Oval Morphology: Dawn-Dusk Asymmetry Partially Induced by Earth's Rotation. *Journal of Geophysical Research: Space Physics*, *128*(6), e2023JA031345. Retrieved from `https://onlinelibrary.wiley.com/doi/full/10.1029/2023JA031345` doi: 10.1029/2023JA031345

Feldstein, Y. I., Gromova, L. I., Grafe, A., Meng, C. I., Kalegaev, V. V., Alexeev, I. I., & Sumaruk, Y. P. (1999, 10). Dynamics of the auroral electrojets and their mapping to the magnetosphere. *Radiation Measurements*, *30*(5), 579–587. doi: 10.1016/S1350-4487(99)00219-X

Feldstein, Y. I., & Starkov, G. V. (1967, 2). Dynamics of auroral belt and polar geomagnetic disturbances. *Planetary and Space Science*, *15*(2), 209–229. doi: 10.1016/0032-0633(67)90190-0

Frey, H. U., Mende, S. B., Carlson, C. W., Gérard, J. C., Hubert, B., Spann, J., ... Immel, T. J. (2001, 3). The electron and proton aurora as seen by IMAGE-FUV and FAST. *Geophysical Research Letters*, *28*(6), 1135–1138. doi: 10.1029/2000GL012352

Gérard, J. C., Hubert, B., Meurant, M., Shematovich, V. I., Bisikalo, D. V., Frey, H., ... Carlson, C. W. (2001, 12). Observation of the proton aurora with IMAGE FUV imager and simultaneous ion flux in situ measurements. *Journal of Geophysical Research: Space Physics*, *106*(A12), 28939–28948. doi: 10.1029/2001JA900119

Harang, L. (1946). The mean field of disturbance of polar geomagnetic storms. *Journal of Geophysical Research*, *51*(3), 353. doi: 10.1029/te051i003p00353

Holzworth, R. H., & Meng, C. I. (1975). Mathematical representation of the auroral oval. *Geophysical Research Letters*, *2*(9), 377–380. doi: 10.1029/GL002i009p00377

Johnsen, M. G. (2013). Real-time determination and monitoring of the auroral electrojet boundaries. *Journal of Space Weather and Space Climate*, *3*, A28. Retrieved from https://www.swsc-journal.org/articles/swsc/full_html/2013/01/swsc130002/swsc130002.html doi: 10.1051/swsc/2013050

Juusola, L., Amm, O., & Viljanen, A. (2006, 5). One-dimensional spherical elementary current systems and their use for determining ionospheric currents from satellite measurements. *Earth, Planets and Space*, *58*(5), 667–678. Retrieved from https://earth-planets-space.springeropen.com/articles/10.1186/BF03351964 doi: 10.1186/BF03351964

Kamide, Y., & Akasofu, S. I. (1983). Notes on the auroral electrojet indices. *Reviews of Geophysics*, *21*(7), 1647–1656. doi: 10.1029/RG021I007P01647

Kervalishvili, G., Stolle, C., Jan, R., & Kauristie, K. (2020). *Data, Innovation, and Science Cluster Swarm-AEBS Description of the Processing Algorithm* (Tech. Rep.). Retrieved from https://earth.esa.int/eogateway/documents/20142/37627/Swarm-AEBS-processing-algorithm-description.pdf

Kilcommons, L. M., Redmon, R. J., & Knipp, D. J. (2017, 8). A new DMSP magnetometer and auroral boundary data set and estimates of field-aligned currents in dynamic auroral boundary coordinates. *Journal of Geophysical Research: Space Physics*, *122*(8), 9068–9079. Retrieved from http://doi.wiley.com/10.1002/2016JA023342 doi: 10.1002/2016JA023342

King, J. H., & Papitashvili, N. E. (2005). Solar wind spatial scales in and comparisons of hourly Wind and ACE plasma and magnetic field data. *Journal of Geophysical Research: Space Physics*, *110*(A2), A02104. doi: 10.1029/2004JA010649

Kisabeth, J. L., & Rostoker, G. (1971, 10). Development of the polar electrojet during polar magnetic substorms. *Journal of Geophysical Research*, *76*(28), 6815–6828. doi: 10.1029/ja076i028p06815

Landry, R. G., & Anderson, P. C. (2019, 3). Empirical Modeling of the Equatorward Boundary of Auroral Precipitation Using DMSP and DE 2. *Journal of Geophysical Research: Space Physics*, *124*(3), 2072–2082. Retrieved from https://onlinelibrary.wiley.com/doi/full/10.1029/2018JA025451 doi: 10.1029/2018JA025451

Laundal, K. M., Finlay, C. C., Olsen, N., & Reistad, J. P. (2018, 5). Solar Wind and Seasonal Influence on Ionospheric Currents From Swarm and CHAMP Measurements. *Journal of Geophysical Research: Space Physics*, *123*(5), 4402–4429. Retrieved from https://onlinelibrary.wiley.com/doi/full/10.1029/2018JA025387 doi: 10.1029/2018JA025387

Laundal, K. M., Østgaard, N., Snekvik, K., & Frey, H. U. (2010, 7). Inter-hemispheric observations of emerging polar cap asymmetries. *Journal of Geophysical Research: Space Physics*, *115*(7), 7230. Retrieved from https://onlinelibrary.wiley.com/doi/full/10.1029/2009JA015160 doi: 10.1029/2009JA015160

Longden, N., Chisham, G., Freeman, M. P., Abel, G. A., & Sotirelis, T. (2010, 9). Estimating the location of the open-closed magnetic field line boundary from auroral images. *Annales Geophysicae*, *28*(9), 1659–1678. Retrieved from www.ann-geophys.net/28/1659/2010/ doi: 10.5194/ANGEO-28-1659-2010

Mende, S. B., Heetderks, H., Frey, H. U., Lampton, M., Geller, S. P., Habraken, S., ... Cogger, L. (2000). Far Ultraviolet imaging from the IMAGE spacecraft. 1. System design. *Space Science Reviews*, *91*(1-2), 243–270. Retrieved from https://link.springer.com/article/10.1023/A:1005271728567 doi: 10.1023/A:1005271728567/METRICS

Mende, S. B., Heetderks, H., Frey, H. U., Stock, J. M., Lampton, M., Geller, S. P., ... Lauche, H. (2000). Far ultraviolet imaging from the image spacecraft. 3. Spectral imaging of lyman-α and OI 135.6 nm. *Space Science Reviews*, *91*(1-2), 287–318. Retrieved from https://link.springer.com/article/10.1023/A:1005292301251 doi: 10.1023/A:1005292301251/METRICS

Milan, S. E., Clausen, L. B., Coxon, J. C., Carter, J. A., Walach, M. T., Laundal, K., ... Anderson, B. J. (2017, 3). *Overview of Solar Wind–Magnetosphere–Ionosphere–Atmosphere Coupling and the Generation of Magnetospheric Currents* (Vol. 206) (No. 1-4). Springer Netherlands. Retrieved from https://link.springer.com/article/10.1007/s11214-017-0333-0 doi: 10.1007/s11214-017-0333-0

Milan, S. E., Provan, G., & Hubert, B. (2007, 1). Magnetic flux transport in the Dungey cycle: A survey of dayside and nightside reconnection rates. *Journal of Geophysical Research: Space Physics*, *112*(A1), 1209. Retrieved from https://onlinelibrary.wiley.com/doi/abs/10.1029/2006JA011642 doi: 10.1029/2006JA011642

Newell, P. T., Feldstein, Y. I., Galperin, Y. I., & Meng, C.-I. (1996, 5). Morphology of nightside precipitation. *Journal of Geophysical Research: Space Physics*, *101*(A5), 10737–10748. Retrieved from https://onlinelibrary.wiley.com/doi/full/10.1029/95JA03516 doi: 10.1029/95JA03516

Newell, P. T., Sotirelis, T., Liou, K., Meng, C. I., & Rich, F. J. (2007, 1). A nearly universal solar wind-magnetosphere coupling function inferred from 10 magnetospheric state variables. *Journal of Geophysical Research: Space Physics*, *112*(1), 1206. Retrieved from https://onlinelibrary.wiley.com/doi/full/10.1029/2006JA012015 doi: 10.1029/2006JA012015

Ohma, A., Madelaire, M., Laundal, K. M., Reistad, J. P., Hatch, S. M., Gasparini, S., ... Walker, S. J. (2023, 6). Background removal from global auroral images: Data driven dayglow modelling. *Earth and Planetary Physics*, *8*(1), 1–11. Retrieved from https://www.eppcgs.org/en/article/doi/10.26464/epp2023051.pdf doi: 10.26464/EPP2023051

Olsen, N. (1996, 12). A new tool for determining ionospheric currents from magnetic satellite data. *Geophysical Research Letters*, *23*(24), 3635–3638. Retrieved from https://onlinelibrary.wiley.com/doi/full/10.1029/96GL02896 doi: 10.1029/96GL02896

Oznovich, I., Eastes, R. W., Huffman, R. E., Tur, M., & Glaser, I. (1993, 3). The aurora at quiet magnetospheric conditions: Repeatability and dipole tilt angle dependence. *Journal of Geophysical Research: Space Physics*, *98*(A3), 3789–3797. Retrieved from https://onlinelibrary.wiley.com/doi/full/10.1029/92JA01950 doi: 10.1029/92JA01950

Redmon, R. J., Peterson, W. K., Andersson, L., Kihn, E. A., Denig, W. F., Hairston, M., & Coley, R. (2010, 11). Vertical thermal O+ flows at 850 km in dynamic auroral boundary coordinates. *Journal of Geophysical Research: Space Physics*, *115*(A11), 0–08. Retrieved from https://onlinelibrary.wiley.com/doi/full/10.1029/2010JA015589https://onlinelibrary.wiley.com/doi/abs/10.1029/2010JA015589https://

agupubs.onlinelibrary.wiley.com/doi/10.1029/2010JA015589 doi: 10.1029/2010JA015589

Rostoker, G., Akasofu, S.-I., Foster, J., Greenwald, R., Kamide, Y., Kawasaki, K., ... Russell, C. (1980). Magnetospheric substorms—definition and signatures. *Journal of Geophysical Research*, *85*(A4), 1663. doi: 10.1029/JA085IA04P01663

Rostoker, G., Friedrich, E., & Dobbs, M. (1996). Physics of Magnetic Storms. *Geophysical Monograph Series*, *98*, 149–160. Retrieved from https://onlinelibrary.wiley.com/doi/full/10.1029/GM098p0149 doi: 10.1029/GM098P0149

Vanhamäki, H., & Juusola, L. (2020). Introduction to Spherical Elementary Current Systems. In *Ionospheric multi-spacecraft analysis tools* (pp. 5–33). Springer International Publishing. doi: 10.1007/978-3-030-26732-2{_}2

Viljanen, A., Juusola, L., Kellinsalmi, M., Käki, S., Nielsen, K., Olsen, N., & Xiong, C. (2020). *Data, Innovation, and Science Cluster Validation of Auroral Electrojet and auroral Boundaries estimated from Swarm observations* (Tech. Rep.). Retrieved from https://earth.esa.int/eogateway/documents/20142/37627/Validation-auroral-electrojet-auroral-boundaries-estimated-from-swarm.pdf

Virtanen, P., Gommers, R., Oliphant, T. E., Haberland, M., Reddy, T., Cournapeau, D., ... Vázquez-Baeza, Y. (2020, 2). SciPy 1.0: fundamental algorithms for scientific computing in Python. *Nature Methods 2020 17:3*, *17*(3), 261–272. Retrieved from https://www.nature.com/articles/s41592-019-0686-2 doi: 10.1038/s41592-019-0686-2

Walker, S., Laundal, K., Reistad, J., Ohma, A., & Hatch, S. (2023, 1). Statistical Temporal Variations in the Auroral Electrojet Estimated With Ground Magnetometers in Fennoscandia. *Space Weather*, *21*(1), e2022SW003305. Retrieved from https://onlinelibrary.wiley.com/doi/full/10.1029/2022SW003305 doi: 10.1029/2022SW003305

Walker, S. J., Laundal, K. M., Reistad, J. P., Hatch, S. M., & Ohma, A. (2022). *Statistics of temporal variations in the auroral electrojets over Fennoscandia- Dataset.* Retrieved from https://zenodo.org/record/6505230#.Yz2FtdJByEA doi: 10.5281/zenodo.6505230

Walker, S. J., Laundal, K. M., Reistad, J. P., Hatch, S. M., Ohma, A., Chisham, G., & Decotte, M. (2023, 9). *A comparison of auroral oval proxies with the boundaries of the auroral electrojets.* Retrieved from https://zenodo.org/record/8318792 doi: 10.5281/ZENODO.8318792

Xiong, C., & Lühr, H. (2014). An empirical model of the auroral oval derived from CHAMP field-aligned current signatures - Part 2. *Annales Geophysicae*, *32*(6), 623–631. Retrieved from www.ann-geophys.net/32/623/2014/ doi: 10.5194/angeo-32-623-2014

Xiong, C., Lühr, H., Wang, H., & Johnsen, M. G. (2014). Determining the boundaries of the auroral oval from CHAMP field-aligned current signatures - Part 1. *Annales Geophysicae*, *32*(6), 609–622. Retrieved from www.ann-geophys.net/32/609/2014/ doi: 10.5194/angeo-32-609-2014

Zou, Y., Nishimura, Y., Lyons, L. R., & Donovan, E. F. (2012, 6). A statistical study of the relative locations of electron and proton auroral boundaries inferred from meridian scanning photometer observations. *Journal of Geophysical Research: Space Physics*, *117*(A6), 6206. Retrieved from https://onlinelibrary.wiley.com/doi/abs/10.1029/2011JA017357 doi: 10.1029/2011JA017357

A comparison of auroral oval proxies with the boundaries of the auroral electrojets

Simon James Walker[1], Karl Magnus Laundal [1], Jone Peter Reistad[1], Anders Ohma[1], Spencer Mark Hatch[1], Gareth Chisham[2], Margot Decotte[1]

[1]Department of Physics and Technology, University of Bergen, Norway
[2]British Antarctic Survey, Cambridge, UK

Key Points:

- We present a new electrojet boundary dataset and compare it with auroral oval proxies
- On average proton aurora boundaries are more aligned with electrojet boundaries than electron aurora boundaries
- Noon and midnight electrojet discontinuities present a problem for auroral oval determination from electrojet boundaries

Corresponding author: Simon Walker, simon.walker@uib.no

Abstract

The boundaries of the auroral oval and auroral electrojets are an important source of information for understanding the coupling between the solar wind and the near-earth plasma environment. Of these two types of boundaries the auroral electrojet boundaries have received comparatively little attention, and even less attention has been given to the connection between the two. Here we introduce a technique for estimating the electrojet boundaries, and other properties such as total current and peak current, from 1-D latitudinal profiles of the eastward component of equivalent current sheet density. We apply this technique to a preexisting database of such currents along the 105° magnetic meridian producing a total of eleven years of 1 minute resolution electrojet boundaries during the period 2000–2020. Using statistics and conjunction events we compare our electrojet boundary dataset with an existing electrojet boundary dataset, based on *Swarm* satellite measurements, and auroral oval proxies based on particle precipitation and field aligned currents. This allows us to validate our dataset and investigate the feasibility of an auroral oval proxy based on electrojet boundaries. Through this investigation we find the proton precipitation auroral oval is a closer match with the electrojet boundaries. However, the bimodal nature of the electrojet boundaries as we approach the noon and midnight discontinuities makes an average electrojet oval poorly defined. With this and the direct comparisons differing from the statistics, defining the proton auroral oval from electrojet boundaries across all local and universal times is challenging.

Plain Language Summary

The global location of the northern and southern lights holds particular importance for understanding where space weather hazards are heightened and where energy from space is deposited in the upper atmosphere. The brightness of these lights and related electrical currents also indicate the magnitude of the energy deposition and associated space weather hazards. However, global imaging of aurora is limited by sunlight, with generally fewer observations during summer months. Furthermore, global observations are not possible from the ground, and space based global imaging has been missing for close to two decades. In this study we investigate alternative methods, with particular emphasis on a technique based on ground magnetometers. Electrical currents have been robustly mapped for two decades over Fennoscandia, without observational limitations due to season. We investigate how the average location of these currents relate to the average location of the aurora and other related current systems. We use these results to discuss the feasibility of finding the location of the aurora from a more abundant data source and increasing the understanding of the underlying mechanisms.

1 Introduction

The boundaries of the auroral oval are natural points of reference for understanding and organising polar ionospheric electrodynamics (Burrell et al., 2020; Kilcommons et al., 2017; Andersson et al., 2004; Redmon et al., 2010). The poleward boundary of the auroral oval is a commonly used proxy of the boundary between open and closed magnetic field lines (OCB) and, therefore, can be used to determine the amount of open magnetic flux contained within the polar cap and is commonly used to describe the magnetic energy stored in the magnetotail (Milan et al., 2007, 2017). The equatorward boundary describes the extent of where this additional energy translates into enhanced auroral activity (precipitation, strengthened auroral electrojets etc.) and is important in understanding where space weather hazards are heightened (Carbary, 2005). The auroral electrojets are often described as flowing within the auroral oval (Johnsen, 2013) and measurements of the electrojets are often reduced to singular metrics to describe the state of polar ionospheric activity (i.e., Auroral Lower index, Auroral Upper index, etc.) (Kamide & Akasofu, 1983; Rostoker et al., 1980).

The auroral oval is typically phenomenologically defined by auroral emissions or through the populations of energetic particle precipitation (Longden et al., 2010; Chisham et al., 2022; Kilcommons et al., 2017; Decotte et al., 2023; Feldstein & Starkov, 1967; Holzworth & Meng, 1975; Zou et al., 2012). Thresholds of the total precipitating electron energy flux are an often used proxy of the OCB (Boakes et al., 2008; Longden et al., 2010). However, ground-based auroral observations, which began prior to the advent of space-based observations, are limited by location and condition requirements, such as clouds, lunar illumination and solar illumination. A number of satellite auroral observations are able to image the entire auroral oval and therefore can provide global boundaries, however they are limited by the time when the satellite was in operation, satellite orbit and to some extent solar illumination because of dayglow (Ohma et al., 2023). Particle detectors onboard satellites, such as the Defense Meteorlogical Space Program (DMSP) satellites, have enabled routine determination of auroral oval boundaries through identification of auroral particle precipitation populations (Kilcommons et al., 2017). An advantage of these measurements is they are not restricted by dayglow and solar illumination but they are limited to point observations along the satellite path. Decotte et al. (2023) have also shown that auroral boundaries identified via DMSP SSJ electrostatic analysers are biased in some local time sectors due to the trajectory of these satellites through the auroral zone.

Both field aligned currents and the auroral electrojets can be estimated from their magnetic field signatures using magnetometers onboard satellites such as CHAllenging Minisatellite Payload (CHAMP) and the *Swarm* satellites and have been compared with the auroral oval (Feldstein et al., 1999; Xiong & Lühr, 2014). Routines have been designed to find the FAC boundaries and electrojet boundaries, with advantages and disadvantages similar to those of boundary estimates made using satellite-based particle instruments (Xiong et al., 2014; Xiong & Lühr, 2014; Aakjær et al., 2016; Juusola et al., 2006; Viljanen et al., 2020; Kervalishvili et al., 2020). Historically, however, estimates of the electrojets have predominantly been made using ground based magnetometers (Harang, 1946). Like satellite magnetometers, ground-based magnetometers are not challenged by weather and solar illumination but additionally have the advantage of being fixed geographically (i.e., can remain in and around the auroral zone and ionospheric interaction region). Such measurements have generally been made at 1-min cadence for the last few decades, and more recently 10-s and even 1-s cadence. However, accurate background magnetic field estimates are required for baseline removal in order to retrieve the real magnitude of perturbations. Additionally, ground magnetometers are limited by location and operation, where more inaccessible sites generally experience more down time and areas of sea or completely inaccessible areas of land produce gaps in the distribution of magnetometers. Furthermore, ground induced currents can obscure the derivation of the ionospheric current particularly when it is assumed the magnetic field perturbations are purely of ionospheric origin.

The clear advantages of ground based magnetometers, in terms of data coverage and reliability, make it important to use the measurements to identify the boundaries of the auroral electrojets and understand their place in describing the auroral oval. Thus enhancing our knowledge of the auroral oval when more typical measurements are lacking and gaining a greater understanding of the links between ionospheric processes. To our knowledge, three studies have used an algorithm based approach to identify the boundaries of the auroral electrojets on the basis of ground magnetometer measurements (Kisabeth & Rostoker, 1971; Johnsen, 2013; Feldstein et al., 1999). In all of these studies the radial component of magnetic field perturbations was primarily used for determination of the latitudinal extent of the auroral electrojets, and in only one of these was a limited comparison with auroral oval boundaries carried out (Feldstein et al., 1999). Kisabeth and Rostoker (1971) used a set of magnetometers around the 302° magnetic meridian (Western Canada), and defined the boundaries of the auroral electrojet as the location of the maxima and minima in the radial component that flank the zero point of the ra-

Boundary Data Set	Boundary Type	Measurements
Current Paper (GBM) (S. J. Walker et al., 2023)	Auroral Electrojets	Ground Based Magnetometers (S. J. Walker et al., 2022; S. Walker et al., 2023)
Swarm (SBM) (Viljanen et al., 2020)	Auroral Electrojets	*Swarm* Magnetometers (Kervalishvili et al., 2020)
SI12 (Chisham et al., 2022)	Aurora	Space Based Imager (IMAGE)
SI13 (Chisham et al., 2022)	Aurora	Space Based Imager (IMAGE)
DMSP (Kilcommons et al., 2017)	Precipitation	Space Based Particle Detector
CHAMP Model (Xiong & Lühr, 2014)	Field Aligned Currents	CHAMP Magnetometer (Xiong et al., 2014)

Table 1: The data sets used in this study, the type of boundaries they identify, and the the measurements used to derive them.

dial component or the peak in the horizontal component. They investigated how the width and peak varied during a selection of substorms. Johnsen (2013) modelled the auroral electrojet as a set of line currents, with amplitudes obtained from fits to the ground magnetic field measured by ground magnetometers in Scandinavia. They then estimated the electrojet boundaries algorithmically using the same criteria described by Kisabeth and Rostoker (1971). These boundaries are then provided to real time tracking and alerts for auroral activity, such as the Advanced Forecast For Ensuring Communications Through Space (AFFECTS) project (Bothmer et al., 2013).

In Section 2 we estimate the electrojet boundaries from minute resolution electrojet current profiles along the 105° magnetic meridian presented by S. Walker et al. (2023) (S. J. Walker et al., 2022), which yields a database spanning a total of eleven years during the 21-year period between 2000 and 2020 (S. J. Walker et al., 2023). In Section 3 we compare these boundaries both in case studies and statistically with auroral electrojet boundaries estimated via satellite-bourne magnetometers, auroral oval boundaries found using particle precipitation measurements from DMSP satellites (Kilcommons et al., 2017; Decotte et al., 2023), a merging electric field scaled model of the FAC boundaries (Xiong et al., 2014; Xiong & Lühr, 2014) and auroral oval boundaries found using satellite based far ultra violet (FUV) measurements of the aurora (Longden et al., 2010; Chisham et al., 2022). In Section 4 we discuss these comparisons and how the auroral electrojet boundaries relate to the auroral oval both on average and on a case by case basis.

2 Data and Methodology

In this section we describe the different boundary datasets used in this study and the methodology behind them. Table 1 summarises these datasets. We also describe the parameters we use to bin our data.

2.1 Electrojet Boundaries from Regionally Constrained Divergence Free Currents

We now describe how we derive the database of electrojet boundaries and properties based on the minute-resolution sheet current density profiles produced by S. Walker et al. (2023).

2.1.1 Estimating the Electrojet Currents

The core component of S. Walker et al. (2023) and how they estimate the divergence-free ionospheric currents is the spherical elementary current systems (SECS) method. The superposition of an appropriately scaled collection of SECS basis functions can recreate any two-dimensional current system that exists on a spherical shell, such as the divergence-free ionospheric currents (Vanhamäki & Juusola, 2020; Amm, 1997; Amm & Viljanen, 1999). Amm (1997) introduced divergence-free SECS basis functions with this purpose in mind, and described the current associated with each type of basis function. Amm and Viljanen (1999) then derived analytic expressions for the corresponding magnetic field. These expressions for the magnetic field enable estimation of the amplitude of each member of a collection of SECS basis functions from measurements of the magnetic field via a linear inverse problem. Once these amplitudes are known, it is straightforward to calculate the total divergence-free current system that can represent the measured magnetic field. S. Walker et al. (2023) used measurements made by a fixed set of twenty ground magnetometers in Fennoscandia to constrain their SECS model along with regularisation of the east-west gradient and the amplitude of the model vector. Using this model, the divergence-free ionospheric sheet current density was estimated along the 105° magnetic meridian for each minute when the magnetometers were available concurrently over the twenty year period from 2000 to 2020 (S. J. Walker et al., 2022).

2.1.2 Electrojet Algorithm

We now describe the algorithm we use to estimate the boundaries and properties of the auroral electrojets (S. J. Walker et al., 2022) from the eastward component of the divergence-free current density for each of the sheet current density profiles described in the previous subsection. Examples of the eastward and westward electrojet boundaries identified via this algorithm are shown in the right middle panels of Figures 1 and 2. These figures show occurrences of DMSP and *Swarm* satellites coinciding with data from S. J. Walker et al. (2022) and a median sheet current density profile is created for each satellite by selecting data from S. J. Walker et al. (2022) that occurs between the time of the boundaries detected by the satellites during the event. Specifically, the algorithm estimates the poleward and equatorward boundary, the value and location of the peak sheet current, and the width and total current of multiple current sections, and proceeds as follows.

1. Initial boundary estimates are identified as the points where the current profile crosses positive or negative thresholds defined as the 10th percentile of the absolute current density or the latitude limits of the meridian (shown as thick black horizontal lines in the right middle panels of figure 1 and 2 as thresholds for the red median profile). This procedure splits the current profile into different sections.
2. Since the current profiles quite often flatten just above the 10th percentile, in the next step the boundary is moved closer to where a clear peak is formed. This point is defined as the closest point to the peak where the gradient is still less than 60% of the mean absolute gradient in the electrojet section. The peak itself is excluded by ensuring that the current magnitude is less than 40% of the mean of the particular section. If a new boundary can not be defined in this way, the initial estimate is kept. As such, the boundaries sometimes end up at or close to the low- and high-latitude edges of the meridian (respectively 49° and 81°). In such cases

the full current section may not have been resolved and the boundaries should not be used.

The boundaries (shown as vertical lines in Figure 1 and 2), peaks, widths, and total integrated current of the three strongest eastward and three strongest westward currents are saved, where the strength is defined by the total integrated current of the profile (the strongest east and west current sections are highlighted in Figure 1 and 2, with their corresponding colour, for the median profiles associated with the *Swarm* A satellite). This dataset is publicly available: S. J. Walker et al. (2023). In this study we use the following criteria to deselect a number of boundaries deemed untrustworthy:

1. Boundaries occurring on first three (less than 50.5° MLat) and last three meridian data points (greater than 79.5°) are removed as the entire current section may not have been resolved
2. Eastward (westward) current sections must have peaks greater than 0.05 $\mathrm{Am^{-1}}$ (less than -0.1 $\mathrm{Am^{-1}}$) for their boundaries to remain. The thresholds are different because the westward electrojet is typically stronger than the eastward electrojet.

2.2 Swarm

We now outline the methodology of Aakjær et al. (2016), which is based on the work of Olsen (1996), for calculating sheet currents using *Swarm* magnetometers. This is the methodology used by Kervalishvili et al. (2020) to produce the publicly available sheet current dataset. That can be obtained from `https://vires.services/` using the code SW_OPER_AEJALPL_2F, SW_OPER_AEJBLPL_2F, and SW_OPER_AEJCLPL_2F for *Swarm* A, B and C respectively. We also describe how Viljanen et al. (2020) and Kervalishvili et al. (2020) use these sheet current profiles to create a data set of Swarm-based electrojet boundaries (also available from `https://vires.services/` using the code SW_OPER_AEJAPBL_2F, SW_OPER_AEJBPBL_2F, SW_OPER_AEJCPBL_2F for *Swarm* A, B and C respectively).

Aakjær et al. (2016) represent the auroral electrojet as a series of line currents at an altitude of approximately 110 km separated by 113 km along and orientated perpendicular to the satellite track. Similar to the SECS approach, the amplitude of each line current is obtained as an inverse problem in which the superimposed magnetic field of the line currents is constrained by the magnitude of the magnetic field perturbations measured by the *Swarm* satellites, where the contribution from FACs is minimal. In Viljanen et al. (2020) these line currents are then transformed into the Quasi-Dipole magnetic east direction before applying the following electrojet algorithm:

1. Find the interpolated zero crossings of the current density curve.
2. Calculate the total current between crossings.
3. Define the electrojet as the series of current densities with the maximum total current or minimum in the case of the westward electrojet.

The dataset is also provided with a set of quality flags that allow for the removal of spurious boundaries. In this study the quality flags were used to remove bad boundaries if any of the following conditions are true:

1. No eastward/westward currents detected.
2. The equatorward boundary occurs at the edge of the analysis area and the density is larger than 20% of peak value.
3. The poleward boundary occurs at the edge of the analysis area and the density is larger than 20% of peak value.

4. the *Swarm* orbit does not fully cover the predefined oval latitude range. The latitude gap is 2 degrees or larger.
5. The equatorward boundary occurs at the edge of the analysis area.
6. The poleward boundary occurs at the edge of the analysis area.
7. The peak value occurs at the edge of the analysis area.

As both an eastward and westward electrojet can be detected in one oval crossing and only the peaks of the electrojets are provided, we choose the appropriate electrojet by the one with the largest peak magnitude.

2.3 Xiong FAC Boundaries

Xiong et al. (2014) use the magnetic field measurements made by CHAllenging Minisatellite Payload (CHAMP) to estimate small-scale field-aligned currents (FACs). They then use these estimates to identify the boundaries of the FACs for each pass of the auroral oval. Xiong and Lühr (2014) bin these boundaries based on MLT and time integrated merging electric field (E_m), with the latter defined in terms of the Newell epsilon value (Newell et al., 2007). For each E_m bin an ellipse is fit to the mean latitude of the poleward and equatorward boundaries across all MLT bins. Each ellipse parameter is represented by a quadratic in terms of E_m, with coefficients estimated using least squares, thus creating a model of the FAC boundaries that is dependent on the Newell epsilon parameter.

2.4 Boundaries from Global Auroral Imagery

Longden et al. (2010) and Chisham et al. (2022) define an algorithm for identifying auroral boundaries in FUV images from the Imager for Magnetopause-to-Aurora Global Exploration (IMAGE) satellite (Mende, Heetderks, Frey, Lampton, et al., 2000). They apply this algorithm to all three imagers on the IMAGE satellite, SI12, SI13 and WIC, creating three datasets. For this study we focus on the boundaries found using the SI12 and SI13 imagers (Mende, Heetderks, Frey, Stock, et al., 2000), which measure emissions related to proton and electron precipitation respectively, as they have a reduced influence from dayglow compared to the WIC imager (Longden et al., 2010). The Chisham et al. (2022) auroral boundary algorithm proceeds as follows: (1) The locations of the pixels of the raw image are found in AACGM (Altitude Adjusted Corrected Geomagnetic) coordinates. (2) Measured intensities in the image are subdivided into bins of size 1 h in MLT, the first bin being 0–1 MLT, and 1° MLat between 50° and 90° MLat. (3) A latitudinal intensity profile is constructed for each MLT segment. (4) This profile is then fitted by two different functions: the sum of a Gaussian function and a quadratic, and the sum of two Gaussian functions and a quadratic. The function with better goodness of fit is then chosen as the better fit. (5) In the case of a single Gaussian being the better fit the poleward and equatorward boundaries are determined by the peak of the Gaussian curve plus and minus the full width at half maximum (FWHM) of the Gaussian respectively. In the case of the double Gaussian the poleward boundary is determined by the peak of the Gaussian curve with the poleward maximum plus its FWHM and the equatorward boundary is determined by the peak of the Gaussian curve with the equatorward maximum minus its FWHM. Additional acceptance criteria for a successful boundary determination can be found in Longden et al. (2010) and Chisham et al. (2022).

2.5 DMSP (Kilcommons Algorithm)

The Kilcommons et al. (2017) algorithm estimates the auroral oval boundaries on the basis of precipitation measurements made by the Special Sensor J (SSJ) instrument onboard DMSP satellites. Decotte et al. (2023) use a portion of this algorithm to produce auroral precipitation occurrence probability maps from the same measurements.

Using the total energy flux of electrons between 1.3 and 30 keV (J_E), Kilcommons et al. (2017) identify candidate auroral ovals as regions where J_E is greater than 10^9 eV for polar passes that cross the auroral oval in two places. Using a figure of merit an auroral oval pair is selected from the candidates and the latitude limits recorded as auroral oval boundaries. Examples of these boundaries can be seen in the top right panel of Figure 1 and 2 along with the J_E latitude profile.

Decotte et al. (2023) used a similar approach however, they use a limit of 2×10^9 eV. Furthermore, to counter problems due to orbital bias and make a dataset that can be statistically compared to the others mentioned in the prior subsections, the threshold is used to create a binary dataset of spacecraft locations (for several DMSP satellites) defined as being within either auroral or non auroral precipitation. From this dataset statistical maps of auroral precipitation occurrence probability are then created.

2.6 Newell coupling function ϵ_N

We make use of the Newell coupling function

$$\epsilon_N = v^{4/3}\left(\sqrt{B_y^2+B_z^2}\right)^{2/3}\sin^{8/3}\left(\theta/2\right), \tag{1}$$

throughout this study. Here v, B_y, B_z, and $\theta=\tan^{-1}\left(B_y/B_z\right)$ are respectively the solar wind speed, the y and z components of the interplanetary magnetic field (IMF), and the IMF clock angle, with all quantities given in geocentric solar magnetic coordinates.

We use ϵ_N averaged over a two-hour backward-looking window, $\bar{\epsilon}_N$, as an indicator of solar wind driving. This quantity is calculated using solar wind and IMF measurements from the NASA OMNI database at one-minute resolution (King & Papitashvili, 2005).

3 Results

3.1 Conjunctions

In this section we present two conjunction events between DMSP satellites, *Swarm* satellites and the 105° magnetic meridian, on which the ground based magnetometer (GBM) electrojet boundary dataset is located.

Figure 1 shows a conjunction between the 105° magnetic meridian, the *Swarm* A and C satellites and the DMSP F17 satellite for the period between 14:33:00 and 14:53:00 on 13^{th} March 2014. Figure 2 shows a conjunction between the 105° magnetic meridian, the *Swarm* A satellite and the DMSP F18 satellite between 16:14:22 and 16:37:34 on the 22^{nd} of February 2014. In both Figures 1 and 2, the left panel shows a map illustrating the 105° meridian and the orbital trajectory of the satellites in a cubed-sphere projection during the conjunction. The top right panel shows the integrated energy flux between 1.3 and 30 keV for the electrons and ions based on measurements by the SSJ instrument onboard the DMSP satellite, together with the precipitation boundaries from Kilcommons et al. (2017). The horizontal line represents the threshold value used by Kilcommons et al. (2017). The middle right panel shows several sheet current density profiles, one for each satellite in the event. Each profile is constructed by finding the median sheet current density in S. J. Walker et al. (2023) occurring at times between when the two boundaries were identified by the particular satellite and are colour coded by the associated satellite (following the scheme in the left panel). Thus there are three median profiles in Figure 1 and two median profiles in Figure 2. The algorithm described in section 2.1.2 is applied to each median profile and the boundaries of the strongest east and west

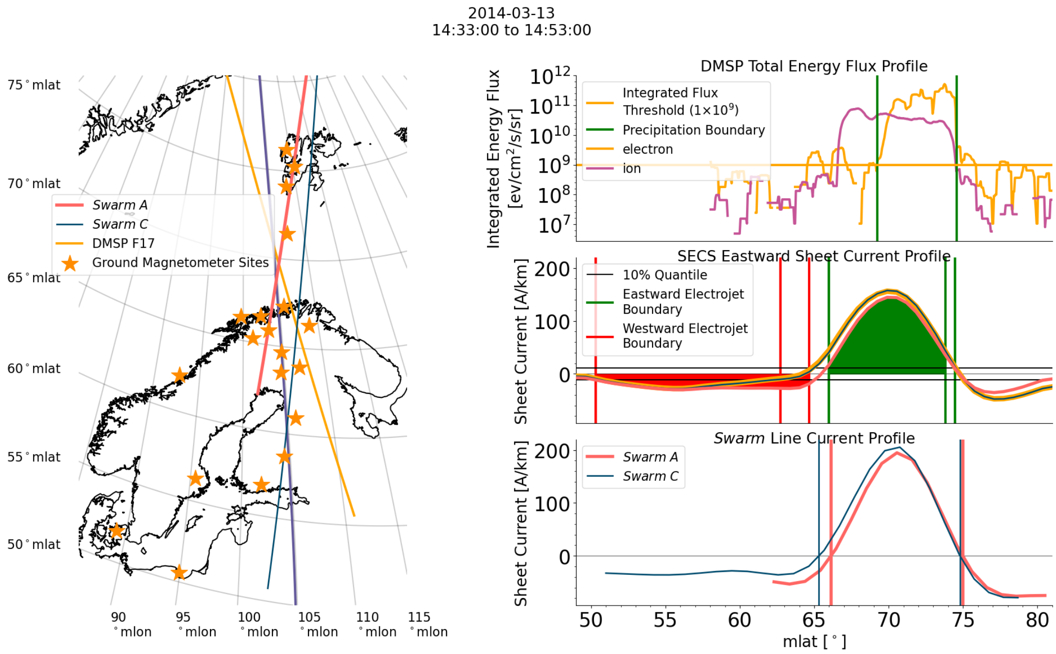

Figure 1: Conjunction event between the 105° magnetic meridian, *Swarm* A, *Swarm* C and DMSP F17, occurring between 14:33:00 and 14:53:00 UT on 13^{th} of March 2014. The 105° magnetic meridian goes from approximately 16.5 to 16.9 MLT and $\bar{\epsilon}_N$ ranges from 3.6 to 4.3. The left panel shows a map of Fennoscandia and the location of the twenty magnetometers used by S. Walker et al. (2023), the satellite trajectories and the 105° magnetic meridian. Magnetic latitudes and longitudes are given in Apex coordinates. The top right panel shows the proton and electron energy flux measurements by DMSP F17 integrated between 1.3 and 30 keV. Vertical green lines show the auroral oval boundaries found through the method described by Kilcommons et al. (2017) and a horizontal orange line shows the associated integrated flux threshold. The middle right panel shows an application of the algorithm, described in section 2.1.2, to three median sheet current density profiles. Each median sheet current density profile is constructed by finding the median of the eastward sheet current density in S. J. Walker et al. (2022) between the time of the boundaries found using DMSP F17, *Swarm* A and *Swarm* C. The colour of each median profile indicates which satellite boundary times are used for the window to determine the median profile, following the same colour convention as the left panel. The strongest east and west current sections found using the median profile associated with *Swarm* A are highlighted with their corresponding colour. The bottom right panel shows the sheet current density profiles found using *Swarm* A and C and their associated electrojet boundaries (Viljanen et al., 2020; Kervalishvili et al., 2020). The colour of the profiles and corresponding boundaries are the same colour to identify the satellite used.

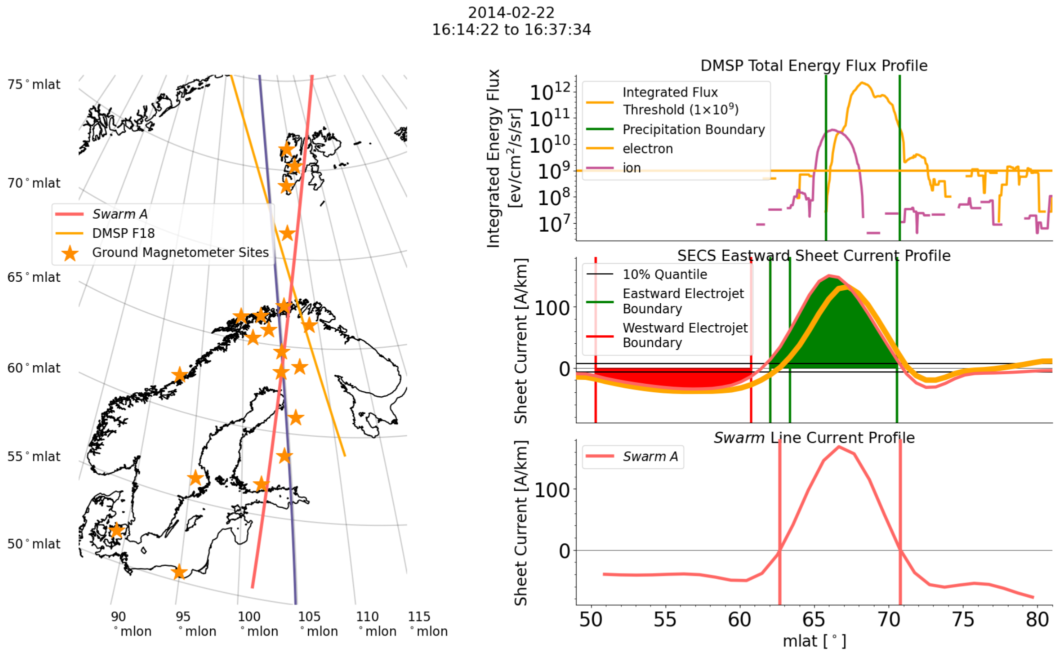

Figure 2: Conjunction event between the 105° magnetic meridian, *Swarm* A and DMSP F18, occurring between 16:14:22 and 16:37:34 UT on 22^{nd} of February 2014, in the same format as Figure 1. The 105° magnetic meridian goes from approximately 18.2 to 18.6 MLT and $\bar{\epsilon}_N$ has a range of 5.4 to 6.1.

current for each median profile are shown with green and red vertical lines respectively. The 10% quantile, which is used for the boundary first guess (cf. section 2.1.2), is shown and the strongest east and west currents are highlighted with their corresponding colours for the median profile associated with the *Swarm* A conjunction in Figure 1 and 2. The bottom right panel shows the sheet current density profiles, derived using the line current method and the *Swarm* magnetometers, and the boundaries of the eastward current (Aakjær et al., 2016; Viljanen et al., 2020; Kervalishvili et al., 2020).

In both conjunctions we find a clear similarity between the SECS derived eastward current, based on ground magnetometers, and the line current derived eastward currents, based on *Swarm* magnetometers. Unsurprisingly, we also see that the boundaries from the two electrojet datasets are very similar particularly if one considers the separation of the data points for the GBM electrojet boundaries, approximately 0.65° MLat. In both conjunctions we find the DMSP poleward boundary to coincide with the poleward electrojet boundaries, but the equatorward boundary is situated close to the peak of the electrojet. The equatorward extent of the integrated ion flux above the threshold matches well with the equatorward boundary of the electrojet, but the poleward extent only matches with the poleward boundary of the electrojet in Figure 1. Despite the short time scale of the conjunctions, the electrojet is not constant. In Figure 1 there is approximately ten minutes separation between the boundaries produced by *Swarm* A and C. Both the associated median GBM current and *Swarm* based magnetometer (SBM) current show clear differences, but the GBM and SBM poleward boundaries are relatively stable over this time period. However, the *Swarm* C and DMSP F17 boundaries are approximately two minutes apart which is why they have near identical median GBM current profiles and the boundaries found from these current profiles are identical. In Figure 2 the *Swarm* A and DMSP F18 boundaries are approximately 10 minutes apart which may contribute

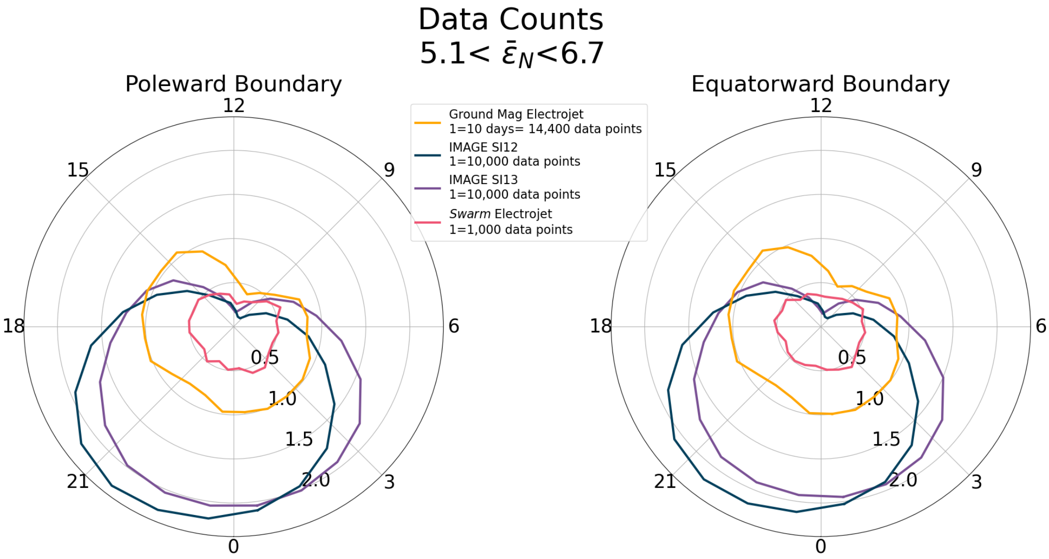

Figure 3: Data coverage and distribution of the SI12, SI13, SBM electrojet and GBM electrojet boundaries from one $\bar{\epsilon}_N$ bin, from Figure 5 and 6, and using the same MLT binning as used in Figure 5 and 6. The left panel shows the data distribution for the poleward boundary and the right panel shows the data distribution for the equatorward boundary.

to significantly different median GBM current profiles and clear differences in the equatorward GBM boundary. But, once again, the poleward boundary shows stability over this period and is identical for the median GBM current profiles associated with DMSP F18 and *Swarm* A.

3.2 Data Availability and Distribution

In the following section we present and describe a statistical investigation of the various boundary datasets.

Six bins of close to equal sample size have been created using $\bar{\epsilon}_N$ for the ground based magnetometer electrojet boundary dataset. These bins are applied to all the datasets and additionally binned by MLT bins of size 1 h starting at 0–1 MLT. The mean Newell epsilon values and binning are explained further in section 3.3. Figure 3 shows the number of poleward and equatorward boundaries that contribute to the $5.1 < \bar{\epsilon}_N < 6.7$ bin for all datasets. The general MLT trend and relative difference between the data sets is not greatly different between the different $\bar{\epsilon}_N$ bins used in Figures 5 and 6. There are much fewer SBM boundaries compared to other datasets and all four datasets show a reduction in the number boundaries pre-noon, however this reduction is much more significant with the FUV boundaries. The difference in the counts between the poleward and equatorward boundaries is minimal for all datasets. There is also a reduction in the number of GBM boundaries between 20 and 23 MLT and, although we do not show these plots, a similar behaviour can be observed for weaker $\bar{\epsilon}_N$ for the SBM boundaries.

Figure 4 shows the median absolute deviation (MAD) of the poleward and equatorward boundaries, as the radial value (in degrees), for the same $\bar{\epsilon}_N$ range as used in Figure 3, in order to depict the spread of the distribution behind each statistic. In general, including the bins not shown, the MAD of the poleward and equatorward boundary for the electrojet boundaries are very similar, particularly in terms of the location

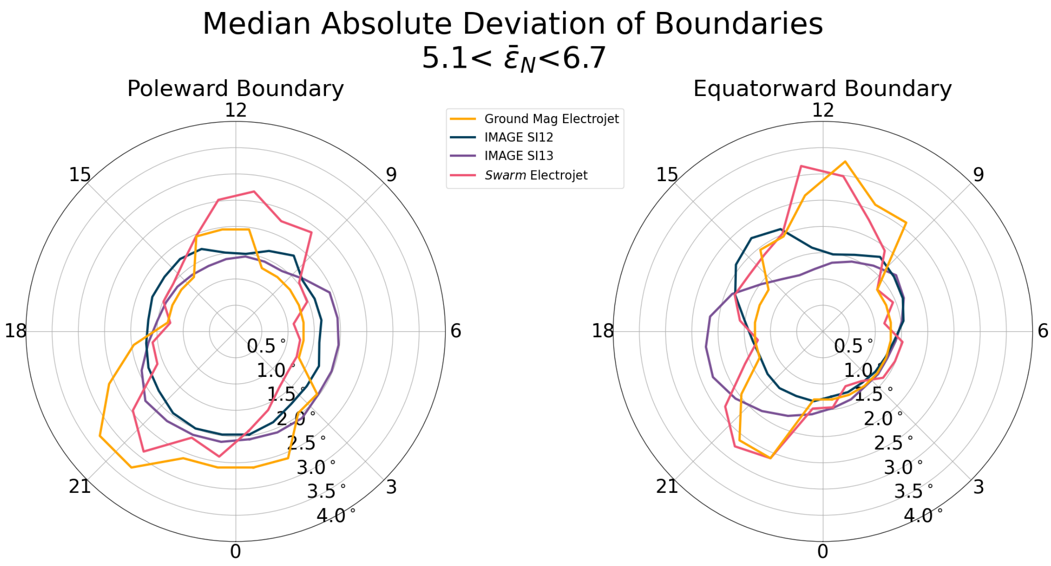

Figure 4: Same as Figure 3 but the median absolute deviation (MAD) is calculated instead of the data counts in each MLT bin.

of the peaks. The same cannot be said for the MAD of the SI12 and SI13 boundaries which exhibit peaks at 15 and 18 MLT respectively for the equatorward boundary but no clear peaks for the poleward boundary. Furthermore, the peaks in the MAD of the poleward boundary and equatorward boundary for all datasets is consistent across all bins of $\bar{\epsilon}_N$. Overall the FUV boundaries have a smaller MAD than the other datasets, most significantly where the MAD peaks in GBM and SBM boundaries between 9 and 12 MLT and 20 and 23 MLT. However the MAD of the equatorward boundaries is comparable between 14 and 18 MLT and between 3 and 9 MLT and where the MAD of the FUV poleward boundaries peak their MAD is the largest of the datasets.

3.3 The dependence of average boundaries on solar wind coupling

We now present and describe the statistical maps (median values) of the different boundary datasets introduced in section 2.

Figure 5 shows the median equatorward and poleward auroral boundaries using the SI12 and SI13 imagers on IMAGE (Chisham et al., 2022) as blue and purple lines respectively, together with the median ground based magnetometer (GBM) electrojet boundaries (this study) shown with orange lines. The auroral occurrence probability based on the SSJ instrument onboard the DMSP satellites (Kilcommons et al., 2017; Decotte et al., 2023) is shown in grey-scale. Each plot within the figure represents a different $\bar{\epsilon}_N$ bin, reflecting its value averaged over the two hours prior to the boundary detection. The limits have been chosen so that the number of GBM electrojet boundaries is similar in each bin. Six bins have been created but the final bin ($\epsilon_N > 9.1$) is omitted due to its large range and having comparatively more anomalous data. The IMAGE boundaries are selected when there are at least four boundaries available for an image, to avoid spurious boundaries. In addition to the algorithm described in section 2.1.2, the electrojet boundaries in Figure 5 are further screened to ensure confidence in the boundaries we present: (1) For each minute of data in S. J. Walker et al. (2022) the electrojet boundaries are defined as the boundaries identified for the strongest current section (where strength is defined as the absolute total current of the section). (2) The boundaries of the elec-

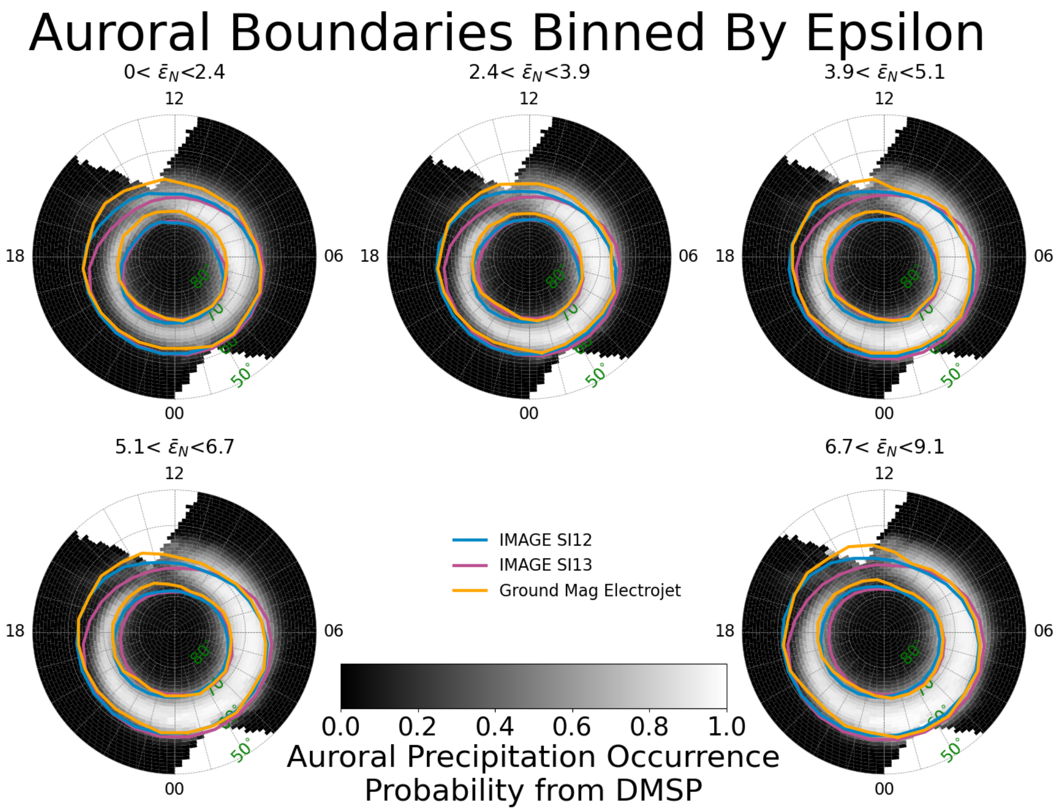

Figure 5: Median SI12, SI13 and GBM electrojet boundaries in 5 bins of $\bar{\epsilon}_N$ (see section 2.6) and in 24 MLT bins of size 1 h, with the first bin being 0-1 MLT. The background colour is used to show the auroral precipitation occurrence probability found by Decotte et al. (2023) and using their spatial bins and additionally binned by our $\bar{\epsilon}_N$ ranges.

trojet are checked for their proximity to the edge of the meridian, those occurring on the first three data points of the meridian (less than 50.5° MLat) and the last three data points (greater than 79.5° MLat) are removed to ensure that the boundary of the electrojet can be seen in S. J. Walker et al. (2022). (3) When an eastward electrojet is chosen the peak must be larger than 0.05 A/km and for a westward electrojet the peak must be below -0.1 A/km. (4) Finally, to make the boundaries comparable to those produced by Chisham et al. (2022) we bin the electrojet boundaries using MLT bins of width 1 MLT, centred at half MLTs. Additionally, we have used used bootstrapping to calculate how well defined the median of the datasets are. This is done using the scipy bootstrap function (Virtanen et al., 2020) where the use of default values creates 9999 random realisations of the data (all the data that contributes to one median data point in Figure 5) each the same size as the initial data. The median is then found for each realisation producing 9999 realisations of the median and then the standard deviation is calculated using these medians which we refer to as the bootstrapped standard deviation of the median from hereafter. We do not show the bootstrapped standard deviation of the median as the values are small. SBM has the largest bootstrapped standard deviations of all the dataset but, even so, the values do not exceed half a degree and therefore the medians of each dataset can be considered well defined. However this should not be considered an indication of the spread of the distributions of the datasets, which is quantified by the MAD values in Figure 4, and further explored in section 4.

We see a remarkable similarity between the SI12 boundaries and the electrojet boundaries in most MLT sectors, however, differences are apparent in the pre-midnight sector and around 15 MLT. In general for both boundaries SI12 is closer to the electrojets in comparison to the auroral occurrence probability and SI13. As $\bar{\epsilon}_N$ increases the SI12 and electrojet boundaries on the dayside become closer but in the pre-midnight sector they become further apart, in this sector the SI12 boundaries remain quasi circular but the GBM boundaries increasingly deviate towards a straight line as $\bar{\epsilon}_N$ increases.

Figure 6 shows median boundaries for the GBM electrojets and the *Swarm* based magnetometer (SBM) electrojets, as purple and orange lines respectively, using the same MLT and $\bar{\epsilon}_N$ bins as in Figure 5. The same auroral occurrence probability maps are also shown. The FAC boundary model (Xiong & Lühr, 2014) is shown as a blue dashed line, where the midpoint of the $\bar{\epsilon}_N$ bin is used as input for the model. As stated previously the bootstrapped standard deviation of the datasets presented are small and thus the median boundaries in Figure 6 are well defined.

The different electrojet boundary datasets show a significant similarity for most MLT and $\bar{\epsilon}_N$ bins but the largest deviations appear on the night side for the poleward boundary and increase with $\bar{\epsilon}_N$. The equatorward boundary of the FAC boundary model shows similarities with the electrojet boundary datasets, however much like FUV boundaries in Figure 5 the FAC and electrojet boundaries are a poorer match in the pre-midnight sector where the shape of the electrojet boundaries change. In general the comparison is much worse between the FAC model and the electrojet boundaries for weaker $\bar{\epsilon}_N$, even more so for the poleward boundary than the equatorward boundary.

3.4 Seasonal variability of median boundaries

Using satellite based FUV images and measurements of particle precipitation, previous studies have investigated how season affects the auroral oval (Oznovich et al., 1993), the OCB (Laundal et al., 2010), and the equatorward boundary of the diffuse aurora (Landry & Anderson, 2019). In this section we investigate how the different boundary datasets used in this study vary with season, with summer and winter defined respectively as when the dipole tilt is $\psi > 10°$ and $\psi < -10°$, since we only use data from the Northern hemisphere.

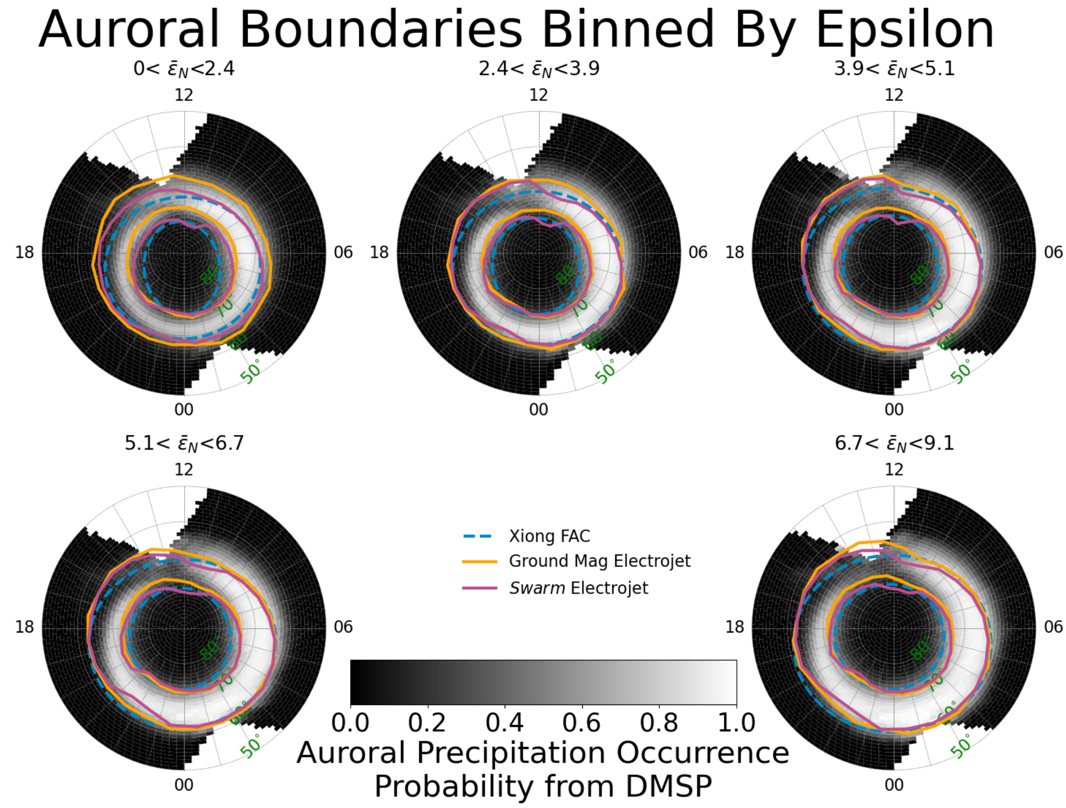

Figure 6: Constructed the same as Figure 5 but using SBM electrojet boundaries instead of SI12 and SI13. Additionally, FAC boundaries are found for each $\bar{\epsilon}_N$ bin by using the midpoint of the bins as input for the model (Xiong & Lühr, 2014).

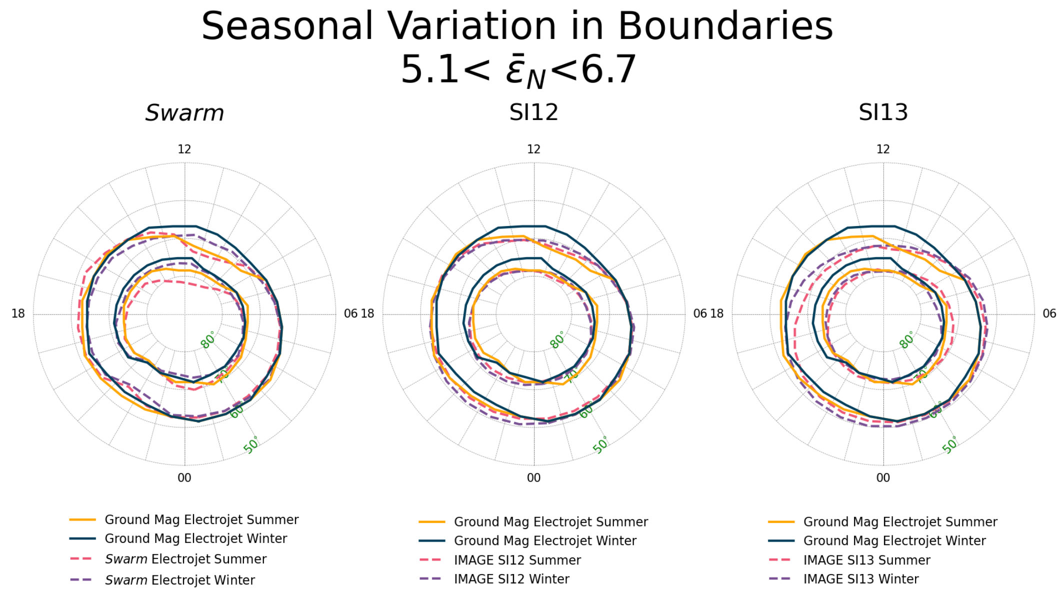

Figure 7: Median SI12, SI13, SBM electrojet boundaries compared with the GBM electrojet boundaries within one $\bar{\epsilon}_N$ bin from Figure 5 and 6 and using the same MLT bins. Boundaries are additionally binned into summer and winter, where summer is defined as when the dipole tilt is greater than 10° and winter is defined as when the dipole tilt is less than -10°. The left panel compares the seasonally binned GBM and SBM electrojet boundaries. The middle panel compares the seasonally binned GBM electrojet boundaries and the SI12 boundaries. The right panel compares the seasonally binned GBM electrojet boundaries and the SI13 boundaries.

Figure 7 shows the median of the poleward and equatorward boundary for each boundary dataset, using the same MLT binning used in Figure 5 and the $5.1 < \bar{\epsilon}_N < 6.7$ bin from the same Figure. From left to right the panel compares seasonal GBM electrojet boundaries with SBM electrojet boundaries, SI12 boundaries and SI13 boundaries respectively, where winter is defined as when the dipole tilt is less than $-10°$ and summer when the dipole tilt is greater than $10°$. We have also calculated the bootstrapped standard deviation for the median boundaries shown, finding that they are typically less than $0.6°$ across all datasets for both summer and winter and the poleward and equatorward boundaries. Once again the SBM boundaries have the largest bootstrapped standard deviation but even the larger spikes do not exceed one degree. Since the GBM dataset is from a fixed geographic location, it has its own inherent dipole tilt relation for a given MLT location, leading to systematic dipole tilt variations in MLT within the allowed summer/winter range. Additionally there exist biases within the distribution of each magnetometer's availability per month that can shift the median month in summer and winter away from the solstices. Hence, subtle seasonal differences should be interpreted with care. The GBM equatorward boundary shows little difference due to season at dawn and from 14 to 17 MLT. However, significant differences can be seen from 8 to 14 MLT and pre-midnight. The GBM poleward boundary shows seasonal differences at all MLT sectors, being closest around 5 MLT and most different around 17 MLT.

In the left panel we can see how the GBM and SBM boundaries compare seasonally. The SBM equatorward and poleward boundaries are similarly affected by season as the GBM boundaries are, in particular we see around 5 MLT that even the different datasets show little difference for both the poleward and equatorward boundaries. In other sectors the datasets are not as good a match. However, the seasonal trend is much the same, where the electrojet is more poleward during the summer in the pre-noon sector and more equatorward from 18 to 24 MLT. The pre-noon sector shows a clear shift in the equatorward boundary of the electrojet during the summer, deviating from the more circular path that is visible during the winter. There is a similar behaviour for the SBM poleward boundaries but not so clearly for the GBM poleward boundaries, an effect that could be attributed to the latitudinal limit of the datasets as the median poeward boundary for the SBM dataset is beyond the latitudinal extent of the GBM dataset.

In the middle panel there is minimal seasonal variation in the SI12 poleward and equatorward boundaries. Therefore, although during summer the SI12 boundaries are similar to the GBM boundaries, in the winter they are not. The biggest difference between the SI12 and GBM equatorward boundaries occurs pre-noon and pre-midnight in both seasons. For the poleward boundary the biggest difference occurs between 11 and 20 MLT during the winter and 13 to 20 MLT in the summer.

In the right panel we see that SI13 has a greater seasonal variation in both boundaries than for SI12. For the equatorward boundary the greatest seasonal variation occurs from noon to midnight but from midnight to noon for the poleward boundary. Although the GBM boundaries do not match as well with SI13 as they do with SI12, there are some MLT sectors where the seasonal trends agree. In the SI12 and 13 datasets in the summer the equatorward boundary pre-noon exhibits a poleward shift and the poleward boundary has a poleward shift from 13 to 21 MLT and an equatorward shift between 1 and 6 MLT.

4 Discussion

Knowledge of the location of auroral oval boundaries is an important tool for understanding space weather and solar wind - magnetosphere coupling (Chisham et al., 2008). In particular, knowledge of the location of the OCB is very useful (Chisham, 2017), and a global and continually available proxy of the OCB would be invaluable. There are challenges associated with finding these boundaries through more conventional measurements such as auroral images and particle precipitation measurements. Here, we have proposed the advantages of understanding the auroral oval through the auroral electrojets due to the temporal and spatial prevalence of ground based magnetometers. In this section we discuss the results presented in section 3, with a focus on how our electrojet boundary dataset compares both statistically and in case studies to *Swarm*-based magnetometer electrojet boundaries (Kervalishvili et al., 2020; Viljanen et al., 2020) and other common means of estimating the auroral oval (SI12, SI13 and auroral precipitation occurrence probability) (Chisham et al., 2022; Decotte et al., 2023; Kilcommons et al., 2017).

In Figure 6 we presented the modelled FAC boundaries (Xiong & Lühr, 2014) together with the median electrojet boundary and auroral occurrence probability maps. One must be careful when interpreting differences between the FAC boundary model, the median boundaries and auroral occurrence probability because the $\bar{\epsilon}_N$ used to constrain the model and the $\bar{\epsilon}_N$ used to bin the boundary data are calculated through different methods (Xiong & Lühr, 2014). Despite this, the trend of increasing eccentricity of the poleward and equatorward boundaries as $\bar{\epsilon}_N$ weakens remains a valid similarity between the FAC boundaries and the SBM and GBM electrojet boundaries. Due to the latitude limit of the GBM electrojet boundaries the increase in eccentricity is clearer for the SBM electrojet poleward boundary than the GBM electrojet poleward boundary. Excluding regions affected by the pre-noon and pre-midnight electrojet discontinuities, it is likely that an ellipse would represent an appropriate geometry for an electrojet boundary model and a similar approach to Xiong and Lühr (2014) could be a fruitful endeavour.

The SBM and GBM electrojet boundaries are similar both statistically (Figure 6) and in the two conjunction studies we present in section 3.1 (Figure 1 and 2). However, at the electrojet discontinuities, around pre-midnight and pre-noon (regions surrounding and including the location of convection reversal), the SBM and GBM electrojet are dissimilar from each other and from the SI12 and SI13 boundary datasets. It is in these regions that we also observe spikes in the MAD of both boundaries from the SBM and GBM datasets (Figure 4), and a dip in the counts (Figure 3). Johnsen (2013) comments on the challenges of determining the electrojet boundaries at these discontinuities due to the elevated complexity of the current systems, and omits these regions from their boundary determination using three- and four-hour universal time (UT) windows for the pre-noon and pre-midnight discontinuities, respectively. However, we see in Figure 5 that on average the electrojet boundaries deviate more from the auroral oval (as defined by SI12) with increasing $\bar{\epsilon}_N$ value and with a greater range of MLTs affected. This suggests that a fixed window is not suitable and that in many cases useful information about the boundaries is likely discarded.

To understand how different boundary datasets are affected in the discontinuity regions, we present in Figure 8 the distribution of the boundaries in two MLT bins around magnetic noon (11–12 MLT and 12–13 MLT) and two MLT bins around pre-midnight (20–21 and 21–22 MLT) for a single $\bar{\epsilon}_N$ bin (5.1–6.7) from Figure 5. There are two peaks in the distribution of GBM and SBM electrojet boundaries, most prominent in the distribution of poleward boundaries, which suggests two distinct populations. Equivalent current maps in S. Walker et al. (2023) show that either side of the discontinuities the strongest current sections are opposite in direction. Consequently, our algorithm will describe the auroral oval using the boundaries of the strongest eastward current section in the afternoon and dusk sectors and using the boundaries of the strongest westward current section in the dawn and morning sectors. In the Harang Discontinuity (HD) a low latitude strong westward (eastward) current flows into a high latitude westward (eastward) current as the discontinuity is traversed clockwise (anti-clockwise) and the opposite is the case for the dayside discontinuity. While in the other MLT sectors the low latitude current section is on average much stronger than the high latitude current section, the strengths become more similar the closer we get to the discontinuities. In our bound-

5.1< $\bar{\epsilon}_N$< 6.7

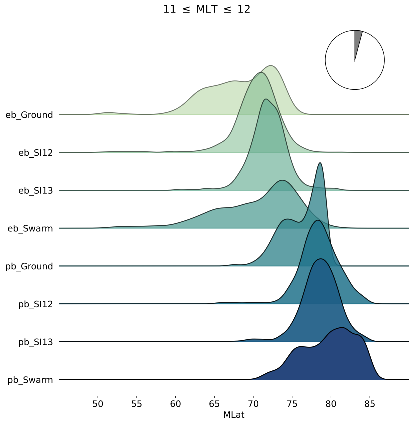

(a) Boundary distributions between 11 and 12 MLT

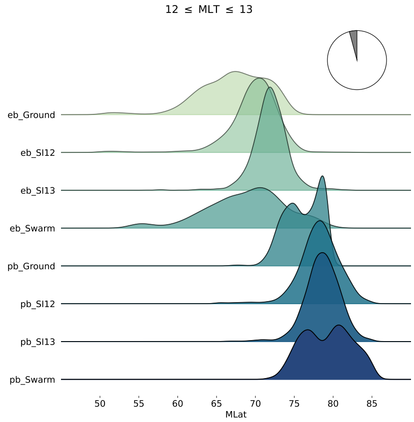

(b) Boundary distributions between 12 and 13 MLT

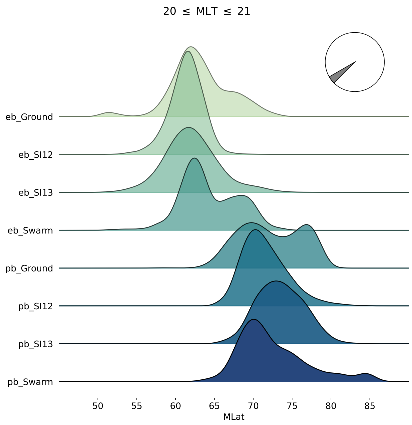

(c) Boundary distributions between 20 and 21 MLT

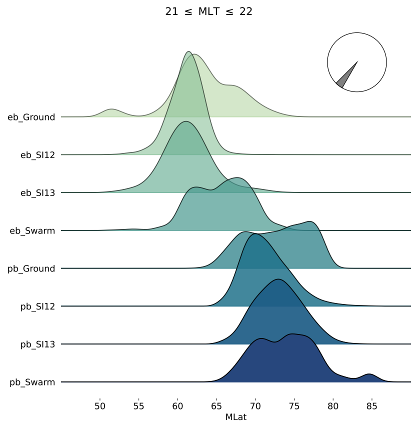

(d) Boundary distributions between 21 and 22 MLT

Figure 8: Distribution of the poleward boundary and equatorward boundary for the SI12, SI3, SBM electrojet and GBM electrojet boundary datasets within one $\bar{\epsilon}_N$ bin from Figure 5 and 6. Four MLT bins are selected from Figure 5 and 6, 11 to 12 MLT (a), 12 to 13 MLT (b), 20 to 21 MLT (c) and 21 to 22 MLT (d).

aries we observe this as the boundary distributions becoming more bimodal and the average shifting poleward as we come closer to the average location of the discontinuities due to the increase in probability of selecting the high latitude current section.

Given that ambiguity in the dominant current section causes a poleward shift in the average boundaries we can use the poleward shift in the GBM and SBM electrojet boundaries in Figure 5 and 6 to identify where and how often the ambiguity occurs. SBM exhibits a greater poleward shift than the GBM dataset and this is due to the latitude limitations of the GBM data set, a consequence of the latitude distribution of magnetometers in Fennoscandia (S. Walker et al., 2023). We also see in Figure 6 that the ambiguity pre-midnight covers a greater range of MLTs than pre-noon, something that can be the result of a difference in the size of the HD and the dayside discontinuity or/and a difference in the distribution in the MLT location of the two discontinuities. The MLT distribution of the discontinuity on the dayside is expected to depend on the IMF B_y, which strongly controls the plasma flow resulting from dayside reconnection (e.g., Laundal et al., 2018). Further separation by IMF B_y could shed light on the effect of B_y on the GBM/SBM poleward boundary variation. As we can see in Figure 7, the poleward shift in the boundaries at the dayside electrojet discontinuity is enhanced during the summer compared to the winter. However, there appears to be no significant seasonal variation in the effect in the HD region. This difference in seasonal variation between the dayside and the nightside could be an effect of corresponding variations in solar EUV produced conductance, which is more important on the dayside. In terms of the use of the GBM and SBM electrojet boundary datasets as auroral oval proxies one must consider the proximity to the HD and dayside discontinuity, solar wind driving ($\bar{\epsilon}_N$) and dipole tilt in order to determine the likelihood of dominant current section ambiguity.

When analysing Figure 5 we find that the GBM electrojet boundaries, in most MLT sectors, are as close to the SI12 boundaries as they are to the SBM electrojet boundaries, particularly as $\bar{\epsilon}_N$ increases. On the other hand, the SI13 boundaries are only close when the differences between SI12 and SI13 are small. Feldstein et al. (1999) found that the eastward electrojet often extends equatorward of the auroral oval as defined by electron precipitation; this is the same relationship that we observe between the electrojet boundaries and the SI13 boundaries and the auroral occurrence probability. Given that SI12 measures the emissions related to proton precipitation and SI13 measurements are dominated by emissions related to electron precipitation (Coumans et al., 2004; Gérard et al., 2001; Frey et al., 2001), our results and the results of Feldstein et al. (1999) therefore support one another, and contradict the notion that the electrojets must flow within the auroral oval as defined by electron precipitation (Rostoker et al., 1996).

Although SI13 is related to the precipitation of auroral energy electrons, Figure 5 shows that the auroral precipitation occurrence probability maps do not everywhere align well with the SI13 boundaries, in particular in the pre-noon sector where the auroral precipitation occurrence probability extends far equatorward of all the boundary datasets in this study. In general the SI13 boundaries and the auroral precipitation occurrence probability become more dissimilar for weaker $\bar{\epsilon}_N$ values but the opposite is the case in the pre-noon sector. Figure 1 and 2 occur in the MLT ranges 16.5–16.9 and 18.2–18.6 and with $\bar{\epsilon}_N$ ranges of approximately 3.6–4.3 and 5.4–6.1, respectively.

Although Feldstein et al. (1999) do not examine the latitude limits of auroral energy proton precipitation they do comment on the peak in proton precipitation occurring close to the centre of the eastward electrojet. Similarly, in Figure 1 and 2 we find the centre of enhanced auroral energy proton precipitation occurs around the centre of the eastward electrojet. Both in the median boundaries (Figure 5) and in the first conjunction (Figure 1) we observe an extension of the relationship between the eastward electrojet and proton precipitation, where limits of the precipitation are close to or coincident with the eastward electrojet boundaries. Figure 1 and 2 show the same as Feldstein et al. (1999) and the median boundaries, that the eastward electrojet can extend equatorward of the electron precipitation defined auroral oval. However, the poleward limit of the electron precipitation occurring close to the poleward boundary of the eastward electrojet that can be see in Figures 1 and 2 is not shown in Figure 5 or in Feldstein et al. (1999) but is seen for the westward electrojet in Figure 5 and Feldstein et al. (1999). Finally, in Figure 2 the latitudinal extent of the proton precipitation poorly reflects the electrojet boundaries. Despite this, the equatorward boundary of the proton precipitation is much closer to the electrojet boundary than for the electron precipitation. Feldstein et al. (1999) finds a large variation in the relationship between precipitation regions and boundaries and the electrojet boundaries and centres, something that is also clear in this study with the difference between patterns in the average boundaries (Figure 5), and the direct comparisons (Figure 1 and 2). A greater number of direct comparisons may be required to ensure the trends in the average boundaries are representative of the trends in reality. In summation, with the results presented one must be careful when interpreting the auroral oval boundaries derived from the electrojet boundaries based on what is seen in the trends of the average boundaries.

5 Conclusion

Finding the boundaries of the auroral oval is of key importance in understanding the region of enhanced space weather hazards in the polar regions. In particular the OCB allows us to quantify the amount of open flux in the polar cap and subsequently understand the amount of energy stored in the magnetotail. In this study we have developed an algorithm that, among other properties, detects the boundaries of the auroral electrojets. Taking advantage of the eastward sheet current density profiles produced by S. Walker et al. (2023), we have created a dataset through the use of our algorithm that spans twenty years and, due to data gaps, totals eleven years with minute cadence. We make this dataset publicly available due to the large range of applications that go beyond the scope of this paper.

The goal of our study was to understand the feasibility of an auroral oval boundary proxy based on our electrojet boundaries. We have found that the auroral oval described through proton and electron precipitation, and their associated FUV aurora, can be variable. Even the comparison between the median boundaries from SI13 images and electron precipitation measurement-based auroral occurrence probability can be significantly variable. As such the relationship between the electron precipitation auroral oval and the electrojet boundaries and the relationship between the proton precipitation auroral oval and electrojet boundaries is very different. We find the proton precipitation auroral oval boundaries are much more coincident with the electrojet boundaries. Consequently, we find that the electrojets can flow outside the electron precipitation auroral oval which agrees with Feldstein et al. (1999) but, as the auroral oval is more typically described by electron precipitation (Kilcommons et al., 2017; Newell et al., 1996; Feldstein & Starkov, 1967), this is contrary to the general description of the ionosphere.

If we move to the paradigm of describing the auroral oval through proton precipitation we can see that there is indeed on average a close resemblance between the auroral oval and the electrojet boundaries. However, determination of the auroral oval from the electrojet boundaries encounters three key challenges: (1) Increasing dominant current section ambiguity with proximity to the electrojet discontinuities makes electrojet boundaries in the pre-noon and pre-midnight sectors a very poor proxy of the auroral oval. (2) The similarities between the electrojet boundaries and the auroral oval boundaries show a seasonal and reconnection rate ($\bar{\epsilon}_N$ value) dependence. (3) While the auroral oval and electrojet boundaries are statistically similar, analysis of conjunctions shows that even under favourable conditions and locations the truth does not always match the average.

Finally, while we are not the first to find the electrojet boundaries on a routine basis (Johnsen, 2013; Viljanen et al., 2020), we are the first to provide a publicly available dataset that is based on ground magnetometers with a significant temporal advantage over those produced from measurements by the *Swarm* satellites. The global shape of the electrojet and its relationship with the auroral oval shows to be an important property of polar ionospheric dynamics and simply reducing the electrojet to singular values, such as the AL and AU indices, will significantly hinder understanding of this field (Kamide & Akasofu, 1983; Rostoker et al., 1980) and limit the capabilities of interpreting the auroral oval when global FUV images are not available or are ineffective.

6 Data Availability Statement

The solar wind and interplanetary magnetic field measurements has been downloaded from the OMNI database: `https://cdaweb.gsfc.nasa.gov/sp_phys/data/omni/hro_1min/`. The dataset of electrojet boundaries and properties can be found at (S. J. Walker et al., 2023). The BAS-derived IMAGE auroral boundaries can be found at https://doi.org/10.5285/fa592594-93e0-4ee1-8268-b031ce21c3ca (Chisham, 2022). The dataset of *Swarm* derived electrojet boundaries can be found through `https://vires.services/` (Viljanen et al., 2020).

7 Open Research

Acknowledgments
This work was supported by Research Council of Norway under contracts 223252/F50 and 300844/ F50 and by the Trond Mohn Foundation.

GC was supported by the British Antarctic Survey Polar Science for a Sustainable Planet Programme, funded by the UK Natural Environment Research Council (NERC) as well as the UK NERC directed grant NE/V002732/1.

The authors would like to thank those involved in producing the IMAGE boundary data sets: Peter Boakes, Nicola Longden, Angeline Burrell, Mervyn Freeman, Steve Milan, and Gary Abel.

The original raw IMAGE FUV data were provided courtesy of the instrument PI Stephen Mende (University of California, Berkeley). We thank the PI, the IMAGE mission, and the IMAGE FUV team for data usage and processing tools. The raw image data, and software, were acquired from http://sprg.ssl.berkeley.edu/image/.

We extend our gratitude to the members of the International Space Science Institute (ISSI) International Team project #506 Understanding Mesoscale Ionospheric Electrodynamics Using Regional Data Assimilation for the discussions and insight into the topic of study. We also thank ISSI Bern for hosting the team.

References

Aakjær, C. D., Olsen, N., & Finlay, C. C. (2016, 8). Determining polar ionospheric electrojet currents from Swarm satellite constellation magnetic data. *Earth, Planets and Space*, *68*(1), 1–14. Retrieved from `https://earth-planets-space.springeropen.com/articles/10.1186/s40623-016-0509-y` doi: 10.1186/s40623-016-0509-y

Amm, O. (1997, 7). *Ionospheric Elementary Current Systems in Spherical Coordinates and Their Application* (Vol. 49; Tech. Rep. No. 7). Retrieved from `http://joi.jlc.jst.go.jp/JST.Journalarchive/jgg1949/49.947?from=CrossRef` doi: 10.5636/jgg.49.947

Amm, O., & Viljanen, A. (1999). Ionospheric disturbance magnetic field continuation from the ground to the ionosphere using spherical elementary current systems. *Earth, Planets and Space*, *51*(6), 431–440. doi: 10.1186/BF03352247

Andersson, L., Peterson, W. K., & McBryde, K. M. (2004, 8). Dynamic coordinates for auroral ion outflow. *Journal of Geophysical Research: Space Physics*, *109*(A8), 8201. Retrieved from `https://onlinelibrary.wiley.com/doi/full/10.1029/2004JA010424https://onlinelibrary.wiley.com/doi/abs/10.1029/2004JA010424https://agupubs.onlinelibrary.wiley.com/doi/10.1029/2004JA010424` doi: 10.1029/2004JA010424

Boakes, P. D., Milan, S. E., Abel, G. A., Freeman, M. P., Chisham, G., Hubert, B., & Sotirelis, T. (2008, 9). On the use of IMAGE FUV for estimating the latitude of the open/closed magnetic field line boundary in the ionosphere. *Annales Geophysicae*, *26*(9), 2759–2769. Retrieved from `www.ann-geophys.net/26/2759/2008/` doi: 10.5194/angeo-26-2759-2008

Bothmer, V., Bothmer, & Volker. (2013). AFFECTS - Advanced Forecast For Ensuring Communications Through Space. *EGUGA*, *15*, 2013–11752. Retrieved from `https://ui.adsabs.harvard.edu/abs/2013EGUGA..1511752B/abstract`

Burrell, A. G., Chisham, G., Milan, S. E., Kilcommons, L., Chen, Y. J., Thomas, E. G., & Anderson, B. (2020, 4). AMPERE polar cap boundaries. *Annales Geophysicae*, *38*(2), 481–490. doi: 10.5194/angeo-38-481-2020

Carbary, J. F. (2005, 10). A Kp-based model of auroral boundaries. *Space Weather*, *3*(10), n/a-n/a. Retrieved from `https://onlinelibrary.wiley.com/doi/full/10.1029/2005SW000162` doi: 10.1029/2005SW000162

Chisham, G. (2017, 1). A new methodology for the development of high-latitude ionospheric climatologies and empirical models. *Journal of Geophysical Research: Space Physics*, *122*(1), 932–947. Retrieved from `https://onlinelibrary.wiley.com/doi/full/10.1002/2016JA023235` doi: 10.1002/2016JA023235

Chisham, G. (2022). *Ionospheric boundaries derived from IMAGE satellite mission data (May 2000 - October 2002) - VERSION 2.0 (Version 2.0) [Data set].*

Chisham, G., Burrell, A. G., Thomas, E. G., & Chen, Y. J. (2022, 7). Ionospheric Boundaries Derived From Auroral Images. *Journal of Geophysical Research: Space Physics*, *127*(7). doi: 10.1029/2022JA030622

Chisham, G., Freeman, M. P., Abel, G. A., Lam, M. M., Pinnock, M., Coleman, I. J., … Villain, J. P. (2008, 3). Remote sensing of the spatial and temporal structure of magnetopause and magnetotail reconnection from the ionosphere. *Reviews of Geophysics*, *46*(1). Retrieved from `https://onlinelibrary.wiley.com/doi/full/10.1029/2007RG000223` doi: 10.1029/2007RG000223

Coumans, V., Gérard, J. C., Hubert, B., Meurant, M., & Mende, S. B. (2004, 4). Global auroral conductance distribution due to electron and proton precipitation from IMAGE-FUV observations. *Annales Geophysicae*, *22*(5), 1595–1611. doi: 10.5194/ANGEO-22-1595-2004

Decotte, M., Laundal, K. M., Hatch, S. M., & Reistad, J. P. (2023, 6). Auroral Oval Morphology: Dawn-Dusk Asymmetry Partially Induced by Earth's Rotation. *Journal of Geophysical Research: Space Physics*, *128*(6), e2023JA031345. Retrieved from `https://onlinelibrary.wiley.com/doi/full/10.1029/2023JA031345` doi: 10.1029/2023JA031345

Feldstein, Y. I., Gromova, L. I., Grafe, A., Meng, C. I., Kalegaev, V. V., Alexeev, I. I., & Sumaruk, Y. P. (1999, 10). Dynamics of the auroral electrojets and their mapping to the magnetosphere. *Radiation Measurements*, *30*(5), 579–587. doi: 10.1016/S1350-4487(99)00219-X

Feldstein, Y. I., & Starkov, G. V. (1967, 2). Dynamics of auroral belt and polar geomagnetic disturbances. *Planetary and Space Science*, *15*(2), 209–229. doi: 10.1016/0032-0633(67)90190-0

Frey, H. U., Mende, S. B., Carlson, C. W., Gérard, J. C., Hubert, B., Spann, J., ... Immel, T. J. (2001, 3). The electron and proton aurora as seen by IMAGE-FUV and FAST. *Geophysical Research Letters*, *28*(6), 1135–1138. doi: 10.1029/2000GL012352

Gérard, J. C., Hubert, B., Meurant, M., Shematovich, V. I., Bisikalo, D. V., Frey, H., ... Carlson, C. W. (2001, 12). Observation of the proton aurora with IMAGE FUV imager and simultaneous ion flux in situ measurements. *Journal of Geophysical Research: Space Physics*, *106*(A12), 28939–28948. doi: 10.1029/2001JA900119

Harang, L. (1946). The mean field of disturbance of polar geomagnetic storms. *Journal of Geophysical Research*, *51*(3), 353. doi: 10.1029/te051i003p00353

Holzworth, R. H., & Meng, C. I. (1975). Mathematical representation of the auroral oval. *Geophysical Research Letters*, *2*(9), 377–380. doi: 10.1029/GL002i009p00377

Johnsen, M. G. (2013). Real-time determination and monitoring of the auroral electrojet boundaries. *Journal of Space Weather and Space Climate*, *3*, A28. Retrieved from https://www.swsc-journal.org/articles/swsc/full_html/2013/01/swsc130002/swsc130002.html doi: 10.1051/swsc/2013050

Juusola, L., Amm, O., & Viljanen, A. (2006, 5). One-dimensional spherical elementary current systems and their use for determining ionospheric currents from satellite measurements. *Earth, Planets and Space*, *58*(5), 667–678. Retrieved from https://earth-planets-space.springeropen.com/articles/10.1186/BF03351964 doi: 10.1186/BF03351964

Kamide, Y., & Akasofu, S. I. (1983). Notes on the auroral electrojet indices. *Reviews of Geophysics*, *21*(7), 1647–1656. doi: 10.1029/RG021I007P01647

Kervalishvili, G., Stolle, C., Jan, R., & Kauristie, K. (2020). *Data, Innovation, and Science Cluster Swarm-AEBS Description of the Processing Algorithm* (Tech. Rep.). Retrieved from https://earth.esa.int/eogateway/documents/20142/37627/Swarm-AEBS-processing-algorithm-description.pdf

Kilcommons, L. M., Redmon, R. J., & Knipp, D. J. (2017, 8). A new DMSP magnetometer and auroral boundary data set and estimates of field-aligned currents in dynamic auroral boundary coordinates. *Journal of Geophysical Research: Space Physics*, *122*(8), 9068–9079. Retrieved from http://doi.wiley.com/10.1002/2016JA023342 doi: 10.1002/2016JA023342

King, J. H., & Papitashvili, N. E. (2005). Solar wind spatial scales in and comparisons of hourly Wind and ACE plasma and magnetic field data. *Journal of Geophysical Research: Space Physics*, *110*(A2), A02104. doi: 10.1029/2004JA010649

Kisabeth, J. L., & Rostoker, G. (1971, 10). Development of the polar electrojet during polar magnetic substorms. *Journal of Geophysical Research*, *76*(28), 6815–6828. doi: 10.1029/ja076i028p06815

Landry, R. G., & Anderson, P. C. (2019, 3). Empirical Modeling of the Equatorward Boundary of Auroral Precipitation Using DMSP and DE 2. *Journal of Geophysical Research: Space Physics*, *124*(3), 2072–2082. Retrieved from https://onlinelibrary.wiley.com/doi/full/10.1029/2018JA025451 doi: 10.1029/2018JA025451

Laundal, K. M., Finlay, C. C., Olsen, N., & Reistad, J. P. (2018, 5). Solar Wind and Seasonal Influence on Ionospheric Currents From Swarm and CHAMP Measurements. *Journal of Geophysical Research: Space Physics*, *123*(5), 4402–4429. Retrieved from https://onlinelibrary.wiley.com/doi/full/10.1029/2018JA025387 doi: 10.1029/2018JA025387

Laundal, K. M., Østgaard, N., Snekvik, K., & Frey, H. U. (2010, 7). Interhemispheric observations of emerging polar cap asymmetries. *Journal of Geophysical Research: Space Physics*, *115*(7), 7230. Retrieved from https://onlinelibrary.wiley.com/doi/full/10.1029/2009JA015160

doi: 10.1029/2009JA015160
Longden, N., Chisham, G., Freeman, M. P., Abel, G. A., & Sotirelis, T. (2010, 9). Estimating the location of the open-closed magnetic field line boundary from auroral images. *Annales Geophysicae*, *28*(9), 1659–1678. Retrieved from `www.ann-geophys.net/28/1659/2010/` doi: 10.5194/ANGEO-28-1659-2010
Mende, S. B., Heetderks, H., Frey, H. U., Lampton, M., Geller, S. P., Habraken, S., ... Cogger, L. (2000). Far Ultraviolet imaging from the IMAGE spacecraft. 1. System design. *Space Science Reviews*, *91*(1-2), 243–270. Retrieved from `https://link.springer.com/article/10.1023/A:1005271728567` doi: 10.1023/A:1005271728567/METRICS
Mende, S. B., Heetderks, H., Frey, H. U., Stock, J. M., Lampton, M., Geller, S. P., ... Lauche, H. (2000). Far ultraviolet imaging from the image spacecraft. 3. Spectral imaging of lyman-α and OI 135.6 nm. *Space Science Reviews*, *91*(1-2), 287–318. Retrieved from `https://link.springer.com/article/10.1023/A:1005292301251` doi: 10.1023/A:1005292301251/METRICS
Milan, S. E., Clausen, L. B., Coxon, J. C., Carter, J. A., Walach, M. T., Laundal, K., ... Anderson, B. J. (2017, 3). *Overview of Solar Wind–Magnetosphere–Ionosphere–Atmosphere Coupling and the Generation of Magnetospheric Currents* (Vol. 206) (No. 1-4). Springer Netherlands. Retrieved from `https://link.springer.com/article/10.1007/s11214-017-0333-0` doi: 10.1007/s11214-017-0333-0
Milan, S. E., Provan, G., & Hubert, B. (2007, 1). Magnetic flux transport in the Dungey cycle: A survey of dayside and nightside reconnection rates. *Journal of Geophysical Research: Space Physics*, *112*(A1), 1209. Retrieved from `https://onlinelibrary.wiley.com/doi/abs/10.1029/2006JA011642` doi: 10.1029/2006JA011642
Newell, P. T., Feldstein, Y. I., Galperin, Y. I., & Meng, C.-I. (1996, 5). Morphology of nightside precipitation. *Journal of Geophysical Research: Space Physics*, *101*(A5), 10737–10748. Retrieved from `https://onlinelibrary.wiley.com/doi/full/10.1029/95JA03516` doi: 10.1029/95JA03516
Newell, P. T., Sotirelis, T., Liou, K., Meng, C. I., & Rich, F. J. (2007, 1). A nearly universal solar wind-magnetosphere coupling function inferred from 10 magnetospheric state variables. *Journal of Geophysical Research: Space Physics*, *112*(1), 1206. Retrieved from `https://onlinelibrary.wiley.com/doi/full/10.1029/2006JA012015` doi: 10.1029/2006JA012015
Ohma, A., Madelaire, M., Laundal, K. M., Reistad, J. P., Hatch, S. M., Gasparini, S., ... Walker, S. J. (2023, 6). Background removal from global auroral images: Data driven dayglow modelling. *Earth and Planetary Physics*, *8*(1), 1–11. Retrieved from `https://www.eppcgs.org/en/article/doi/10.26464/epp2023051.pdf` doi: 10.26464/EPP2023051
Olsen, N. (1996, 12). A new tool for determining ionospheric currents from magnetic satellite data. *Geophysical Research Letters*, *23*(24), 3635–3638. Retrieved from `https://onlinelibrary.wiley.com/doi/full/10.1029/96GL02896` doi: 10.1029/96GL02896
Oznovich, I., Eastes, R. W., Huffman, R. E., Tur, M., & Glaser, I. (1993, 3). The aurora at quiet magnetospheric conditions: Repeatability and dipole tilt angle dependence. *Journal of Geophysical Research: Space Physics*, *98*(A3), 3789–3797. Retrieved from `https://onlinelibrary.wiley.com/doi/full/10.1029/92JA01950` doi: 10.1029/92JA01950
Redmon, R. J., Peterson, W. K., Andersson, L., Kihn, E. A., Denig, W. F., Hairston, M., & Coley, R. (2010, 11). Vertical thermal O+ flows at 850 km in dynamic auroral boundary coordinates. *Journal of Geophysical Research: Space Physics*, *115*(A11), 0–08. Retrieved from `https://onlinelibrary.wiley.com/doi/full/10.1029/2010JA015589https://onlinelibrary.wiley.com/doi/abs/10.1029/2010JA015589https://`

agupubs.onlinelibrary.wiley.com/doi/10.1029/2010JA015589 doi: 10.1029/2010JA015589

Rostoker, G., Akasofu, S.-I., Foster, J., Greenwald, R., Kamide, Y., Kawasaki, K., ... Russell, C. (1980). Magnetospheric substorms—definition and signatures. *Journal of Geophysical Research*, *85*(A4), 1663. doi: 10.1029/JA085IA04P01663

Rostoker, G., Friedrich, E., & Dobbs, M. (1996). Physics of Magnetic Storms. *Geophysical Monograph Series*, *98*, 149–160. Retrieved from https://onlinelibrary.wiley.com/doi/full/10.1029/GM098p0149 doi: 10.1029/GM098P0149

Vanhamäki, H., & Juusola, L. (2020). Introduction to Spherical Elementary Current Systems. In *Ionospheric multi-spacecraft analysis tools* (pp. 5–33). Springer International Publishing. doi: 10.1007/978-3-030-26732-2{_}2

Viljanen, A., Juusola, L., Kellinsalmi, M., Käki, S., Nielsen, K., Olsen, N., & Xiong, C. (2020). *Data, Innovation, and Science Cluster Validation of Auroral Electrojet and auroral Boundaries estimated from Swarm observations* (Tech. Rep.). Retrieved from https://earth.esa.int/eogateway/documents/20142/37627/Validation-auroral-electrojet-auroral-boundaries-estimated-from-swarm.pdf

Virtanen, P., Gommers, R., Oliphant, T. E., Haberland, M., Reddy, T., Cournapeau, D., ... Vázquez-Baeza, Y. (2020, 2). SciPy 1.0: fundamental algorithms for scientific computing in Python. *Nature Methods 2020 17:3*, *17*(3), 261–272. Retrieved from https://www.nature.com/articles/s41592-019-0686-2 doi: 10.1038/s41592-019-0686-2

Walker, S., Laundal, K., Reistad, J., Ohma, A., & Hatch, S. (2023, 1). Statistical Temporal Variations in the Auroral Electrojet Estimated With Ground Magnetometers in Fennoscandia. *Space Weather*, *21*(1), e2022SW003305. Retrieved from https://onlinelibrary.wiley.com/doi/full/10.1029/2022SW003305 doi: 10.1029/2022SW003305

Walker, S. J., Laundal, K. M., Reistad, J. P., Hatch, S. M., & Ohma, A. (2022). *Statistics of temporal variations in the auroral electrojets over Fennoscandia- Dataset.* Retrieved from https://zenodo.org/record/6505230#.Yz2FtdJByEA doi: 10.5281/zenodo.6505230

Walker, S. J., Laundal, K. M., Reistad, J. P., Hatch, S. M., Ohma, A., Chisham, G., & Decotte, M. (2023, 9). *A comparison of auroral oval proxies with the boundaries of the auroral electrojets.* Retrieved from https://zenodo.org/record/8318792 doi: 10.5281/ZENODO.8318792

Xiong, C., & Lühr, H. (2014). An empirical model of the auroral oval derived from CHAMP field-aligned current signatures - Part 2. *Annales Geophysicae*, *32*(6), 623–631. Retrieved from www.ann-geophys.net/32/623/2014/ doi: 10.5194/angeo-32-623-2014

Xiong, C., Lühr, H., Wang, H., & Johnsen, M. G. (2014). Determining the boundaries of the auroral oval from CHAMP field-aligned current signatures - Part 1. *Annales Geophysicae*, *32*(6), 609–622. Retrieved from www.ann-geophys.net/32/609/2014/ doi: 10.5194/angeo-32-609-2014

Zou, Y., Nishimura, Y., Lyons, L. R., & Donovan, E. F. (2012, 6). A statistical study of the relative locations of electron and proton auroral boundaries inferred from meridian scanning photometer observations. *Journal of Geophysical Research: Space Physics*, *117*(A6), 6206. Retrieved from https://onlinelibrary.wiley.com/doi/abs/10.1029/2011JA017357 doi: 10.1029/2011JA017357